Experimental testing of full-scale glulam frames with buckling restrained braces

Wenchen Dong[a,*], Minghao Li[a], Chin-Long Lee[a], Gregory MacRae[a], Anthony Abu[a]

[a]*Department of Civil and Natural Resources Engineering, University of Canterbury, New Zealand*

Abstract

This experimental study investigates cyclic performance of a timber-steel hybrid structural system consisting of glulam frames and buckling restrained braces (BRBs). The BRBs are designed as ductile elements in the hybrid system to dissipate energy under seismic loading. Following the capacity design approach, two full-scale 8 m wide and 3.6 m high BRB glulam frame (BRBGF) specimens were tested. The BRBs were connected to the glulam frames by pins and steel gusset plates. Dowelled connections with inserted steel plates were used in one specimen to connect the glulam members while screwed connections with steel side plates were used in the other specimen. The test results showed that the integration of BRBs into the glulam frames significantly improve the load carrying capacity and energy dissipation. Both BRBGF specimens achieved a minimum ductility factor of 3.0 based on CEN method. The connections and the glulam members were well protected without significant damage. Therefore, the dowelled connections and screwed connections provided solutions to engage BRBs efficiently to resist lateral loads in this hybrid system.

Keywords: Seismic performance, glulam frames, buckling restrained braces (BRBs), dowelled connections, screwed connections

1. Introduction

With more availability of high performance engineered timber products, there are increasing interests in building multi-storey engineered timber buildings around the world. The structure design of multi-storey timber buildings is usually governed by lateral loads, especially earthquakes for seismic zones like New Zealand. The beam-column connections in timber frames are normally considered to transmit only the shear force without moment-resisting capacity in current standards due to the brittle failures perpendicular to timber grain and low rotation stiffness caused by oversized fastener holes. Extra structure members are usually required in timber frames to form lateral force resisting systems (LFRS) and timber braces are one of the popular options for LFRS. In conventionally braced timber frames, energy dissipation under seismic loads primarily relies on the connections between the timber braces and the main frames as timber braces are too brittle in tension to dissipate energy. As a consequence, it may cause severe damage to the connections under major earthquakes that is difficult to repair. Besides, because the connections have low energy dissipation capacity, the system ductility is limited. For example, the four-storey Beatrice Tinsley building at the University of Canterbury was designed with a low ductility factor (1.25) for the braced timber frames [1]. The low ductility might cause less economical cross sections and limit the height of timber structures in seismic zones. Therefore, it is beneficial to design multi-storey timber buildings with more ductile LFRS and improved seismic performance. Steel braces may improve system ductility as they can yield and dissipate more energy. However, steel concentrically braced frames may still show limited ductility and overall poor seismic performance due to buckling of the braces in compression [2]. Buckling restrained braces (BRBs) can restrain the buckling of steel braces in compression and achieve similar behaviour under tension and compression. Therefore, the integration of BRBs into timber frames might be a solution to improve the ductility of timber buildings in seismic zones.

*Corresponding author
Email address: wenchen.dong@pg.canterbury.ac.nz (Wenchen Dong)

Extensive experimental studies on BRB component, sub-assemblage and BRB frame (BRBF) have been conducted for steel structures [3, 4, 5, 6, 7, 8, 9, 10]. Watanaba et al. [11] and Takeuchi et al. [12] tested BRBs and provided global and local buckling prevention strategy, respectively. Different forms of BRBs were proposed and tested [13, 14, 15, 16, 17]. It also has been confirmed that most BRBs could sustain stable cyclic performance in the component tests. However, some BRBF tests [18, 19, 20] showed the buckling or welding fracture of gusset plates, which highlighted the importance of conducting system tests on BRBFs. Aiken et al. [18] tested a 0.7-scale one-bay one-storey BRBF with rigid beam-column-brace connections. The results showed crack propagation at the column-gusset plate weld and gusset plate distortion at 2.0% drift ratio, which illustrated that rigid beam-column-brace connections negatively impacted the overall performance. Fahnestock et al. [21] tested a one-bay four-storey BRBF with improved connection details and pinned-end BRBs. The test frame sustained 5.0% drift ratio with minimal damage and no significant strength degradation was observed. Berman and Bruneau [22] tested a 1/3-scale three-storey BRBF with unconstrained gusset connections. The results showed that the unconstrained gusset connections reduced the negative impact of frame action and the base shear force carried by the frame. Various models were developed to represent BRB and BRBF behaviour under cyclic loading as well [23, 24, 25], for instance, the bilinear model [26], the Bouc-Wen smooth law model [27], Ramberg-Osgood model [28], Menegotto-Pinto model [29] and core-spring models [30] for BRBs and fixed joints [26, 28, 31], rigid-offset fixed joints [32] and fully-pinned joints [29] for beam-column connections. It was found that the models predicted the experimental behaviour well.

Research has also been conducted to integrate BRBs to new reinforced concrete (RC) structures and retrofit RC frames as an economical retrofit solution [33, 34, 35, 36, 37, 38, 39]. Special connection details between BRBs and RC frames such as bearing block and cast-in steel brackets were proposed for existing and new constructed RC frames [40], respectively. Numerical models were developed to simulate the performance of the BRBFs [41, 42]. The tests and numerical analysis showed that BRBs improved strength, stiffness and energy dissipation capacity of the RC frames. Therefore, it is promising to integrate BRBs into timber frames as well.

The feasibility of timber-steel hybrid structures was proved by Khorasani [43]. Li et al. [44] conducted a seismic performance assessment for multi-storey steel moment resisting frames infilled with light wood frame shear walls and He et al. [45] carried out shake table tests and numerical simulation for a 2/3-scale timber-steel hybrid system. The results showed that the system achieved desirable seismic performance. Blomgren et al. [46] tested BRBs with timber casings (T-BRBs) and used them in a numerical analysis of a 12-storey timber building. The results showed the feasibility of incorporating BRBs in a mass timber structure but the information on the design method and the connection details was missing. Murphy et al. [47] tested six full-scale T-BRB components. The results showed that they could meet the requirement of AISC341-16 [48] when suitable engineered wood products for casing were chosen. Timmers and Jacobs [49] conducted a comparative study on a high-rise RC building and a high-rise mass timber building containing BRBs by numerical modelling. It was demonstrated that mass timber could provide a viable alternative to RC in high seismic regions. However, further study was required to investigate the behaviour of the critical connections to BRBs. Zhang et al. [50] conducted a shake table test on a half-scale 5-storey post-and-beam glulam frame structure with timber braces and T-BRBs. It was found that the BRBs improved the building performance but the observed failure modes were timber brace splitting and connection buckling. Again, this research emphasized the importance of introducing enhanced connection design to engage BRBs in a timber system. Gilbert and Erochko [51] performed half-scale cyclic tests of a type of timber-steel hybrid beam-column moment connections made of glued-in rods and steel hubs. This connection type can be used to connect BRBs. However, glued-in-rod connections typically require strict quality controls during the manufacturing process and no widely acceptable design method is available [52]. Past research on hybrid timber-steel structures illustrated the importance of timber-steel connections for integrating BRBs into timber frames and there were limited suitable connections for BRBs and timber frames. Timber materials have lower strength and stiffness perpendicular to grain, which causes those connections for steel and RC structures are not suitable for timber structures. Thus, alternative enhanced connections require more investigation for this hybrid system.

Dowel-type connections consisting of bolts or dowels and inserted steel plates are commonly used in heavy timber frames [53]. Design standards such as Eurocode 5 [54] provide detailed design formulas for dowel-type connections with one inserted steel plate based on the Johansen's theory [55]. Brittle failures are avoided by satisfying minimum spacing requirements for most cases. The rotation stiffness was negligible for bolted connections due to the over-sized holes for installation tolerance [56], while the limited moment-carrying capacity could help to avoid the torsion of gusset plates. To achieve higher capacity, more dowels and more inserted steel plates are required. The lateral load-carrying capacity for dowel-type connections with multiple slotted-in steel plates have been validated experimentally [57] and design equations were proposed [58, 59]. Experimental tests of high strength dowelled connections with cross laminated timber (CLT) were conducted. The results showed that dowelled connections were capable to carry high loads as hold-downs for multi-storey timber buildings and the overstrength was derived to avoid brittle failures [60, 61, 62]. However, the connections that used to integrate BRBs are loaded with an angle to the timber grain, which is more complicated and the initial slips of dowelled connections could reduce the efficiency of BRBs. Their effects need to be investigated by further experimental tests. Past research also showed that the stiffness prediction in Eurocode 5 [54] could overestimate the stiffness of multiple fastener connections significantly [63]. The beam-on-foundation models were developed and recommended to estimate the stiffness for dowel-type connections [64] but the modulus of foundation also required further investigation by experimental tests [65]. Connections with self-tapping screws (STS) are another popular option for timber structures due to their economic advantages and easy installation. Bejtka and Blaß [66] exploited the high tensile capacity of STS in glulam by installing inclined STS such that the ultimate load on the joints was not just limited by the embedding strength of the timber member and bending capacity of the fastener, but also the withdrawal capacity of the fastener and friction between the timber members. Furthermore, experimental tests were conducted for inclined STS on timber-timber [67, 68] and steel-timber interface [69, 70, 71, 72] to investigate the influence of inclined angles, number of STS and STS layouts on connection strength, stiffness and ductility. Design equations for strength of inclined STS connections were introduced into Eurocode 5 [54]. Several analytical models were developed for concrete-timber [73], and timber-timber interface [67, 74]. However, effects of cyclic loading on strength and stiffness for timber-steel STS connections are still unknown, especially for load with an angle to the timber grain.

Based on an overview of previous experimental and numerical work above, BRBs can be well represented by previous numerical models developed for steel structures. However, limited studies are available for the connections between BRBs and timber frames. The timber-steel connections need to be specially designed and the information about their performances in the system is missing, which restrained the transfer of knowledge developed for BRBF in steel and RC structures. Therefore, experimental tests are required to understand the overall performance well and develop new numerical models or modified models based on those used for steel and RC structures. In this study, an attempt was made to integrate BRBs to glulam frames to achieve enhanced strength, stiffness, ductility and energy dissipation. Two full-scale BRB glulam frame (BRBGF) specimens were designed with two different connections following the capacity design approach and tested under cyclic loading. The objectives were to assess the cyclic performance of the new hybrid system, check the strength and stiffness of the connections and provide information for future numerical modelling.

2. Design of test specimens

2.1. Prototype building

As shown in Fig. 1, a six-storey glulam office building located in Christchurch, New Zealand, was used as a prototype building to design the BRBGF specimens. According to the literature review, the beam-column connections were assumed as pinned connections to reduce the frame action. The building had CLT roof and floors as rigid diaphragm [75] that transferred lateral loads to its LFRS, BRBGFs. The seismic demand calculation followed the equivalent static method in New Zealand standards NZS 1170.5 [76] and the loading information is listed in Table 1.

Table 1: Loading information of the prototype building

Item	Value	Item	Value
Importance level	2	Return period factor R	1.0
Design working life	50 years	Near-fault factor N	1.0
Annual probability of exceedance	1/500	Dead load on floor	1.8 kPa
Site subsoil class	C	Dead load on roof	1.6 kPa
Hazard factor Z	0.3	Live load	3.0 kPa

The seismic load in the Y direction was resisted by four BRBGFs. The specimens represented one of the BRBGFs on the second storey highlighted in Fig. 1b. The BRBGF on the second storey was chosen because it contained all critical BRB-glulam interface connections including the mid-span connection linking inverted-V BRBs and the top beam (referred as the top connection) and the corner connection linking one BRB with the bottom beam and one side column (referred as the bottom connection). The other reason was that experimental tests [21] and numerical analysis [20, 77] indicated that the peak inter-storey drift might occur in the second storey of multi-storey buildings.

Two BRBGF specimens (S-D and S-S) were designed and tested, as shown in Fig. 2. Both specimens were 8 m wide and 3.6 m high. The two specimens were identical except for the use of different connection details. S-D used dowels and inserted steel plates (referred as the dowelled connections) and S-S used inclined STS and steel side plates (referred as the screwed connections). All material properties used for specimens are listed in Table 2. P-Delta effects were not considered in the specimen design because the column bottom was assumed as the pinned connection and research by Sahoo and Chao [77] indicated that P-Delta effects might not have a significant influence on the overall behaviour of BRBF as long as the lateral drift was well controlled.

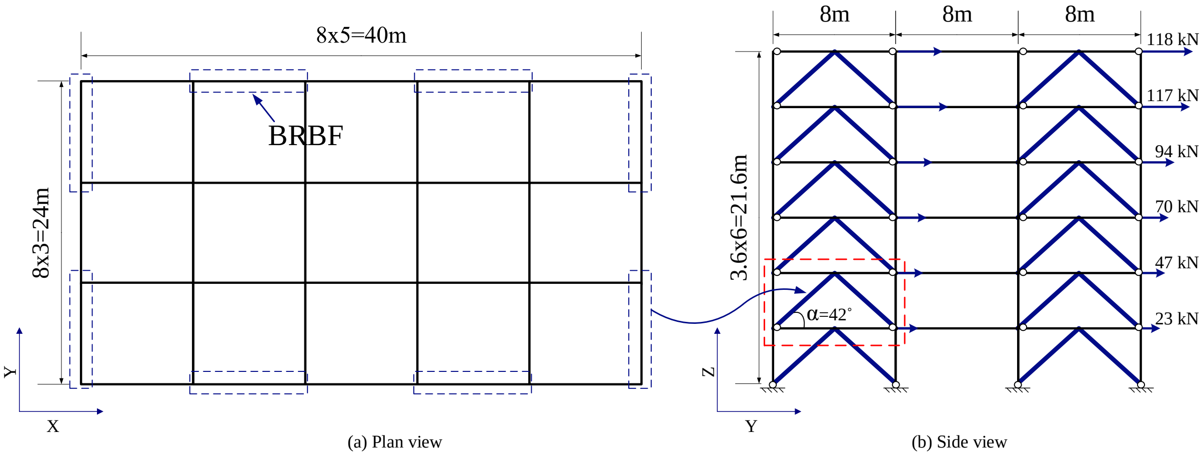

Figure 1: Plan view and side view of the prototype building

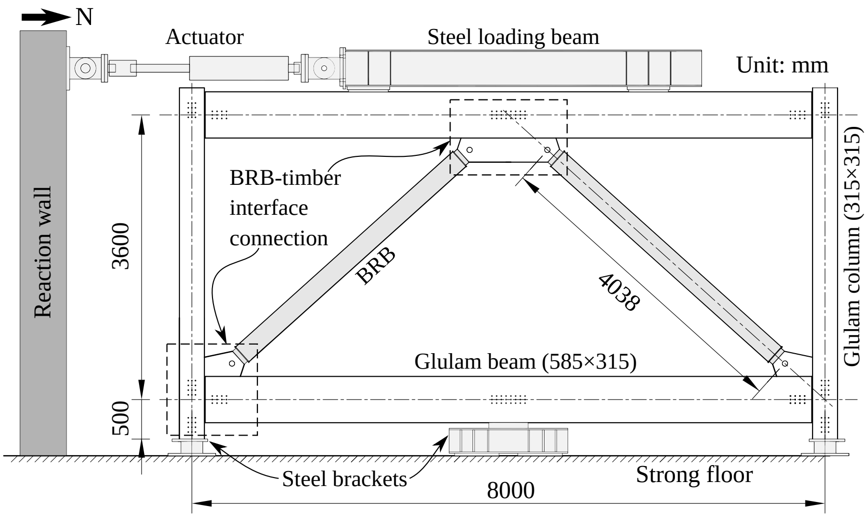

Figure 2: Elevation view of the specimen test setup

Table 2: Material properties

Members	Materials	Properties
BRBs	16 mm-thick Grade 235 flat plate [78]	Nominal yield strength f_{ys} = 235 MPa Modulus of elasticity E_S = 206 GPa Steel core length l_c = 3056 mm Steel core area A_c = 1120 mm^2 Transition length l_{tr} = 120 mm Transition area A_{tr} = 2320 mm^2 Elastic length l_e = 862 mm Elastic area A_e = 8800 mm^2
Beams and columns	GL10 New Zealand Radiata Pine [79]	Bending strength f_b = 22 MPa Compression strength parallel to grain f_c = 26 MPa Tension strength parallel to grain f_t = 11 MPa Compression strength perpendicular to grain $f_{cp,0}$ = 8.9 MPa Shear strength f_s = 3.7 MPa Modulus of elasticity E_{GL} = 10 GPa Modulus of rigidity G_{GL} = 670 MPa Characteristic density ρ_k = 434 kg/m^3 Mean density ρ_m = 466 kg/m^3 Average moisture contents =12%
Gusset plates in S-D	20 mm-thick Grade 300 flat plate [80]	f_{ys} = 300 MPa E_S = 210 GPa
Dowels	ϕ12 Grade 300 round bar	f_{ys} = 300 MPa Tensile strength $f_{u,k}$ = 345 MPa E_S = 210 GPa
Gusset plates in S-S	12 mm-thick Grade 350 flat plate [80]	f_{ys} = 350 MPa E_S = 210 GPa
Screws	$\phi 11 \times 300$ VGS STS [81]	Tensile strength $f_{tens,k}$ = 38 kN Withdrawal parameter $f_{ax,k}$ = 11.7 N/mm^2 Effective diameter d_{ef} = 7.3 mm
Washers	VGU 45° washers [82]	f_{ys} = 235 MPa E_S = 210 GPa

2.2. Capacity design

Following the capacity design approach, the BRBs in this hybrid system are assumed as ductile elements and all glulam members and connections are non-ductile elements protected from significant damage under major earthquakes. Therefore, the glulam members and connections were designed considering overstrength of BRBs. For steel BRBFs, the American steel code AISC 341-16 [48] requires:

$$R_{d,brittle} \geq R_y \omega \beta R_{k,BRB} \tag{1}$$

where, $R_{d,brittle}$ is the capacity of non-ductile members; $R_y = 1.15$ is the material overstrength factor suggested by AISC 341-16 [48]; ω is the BRB strain hardening adjustment factor; β is the BRB compression strength adjustment factor; $R_{k,BRB} = f_{ys} A_c$ is the characteristic yield capacity of BRB and A_c is the cross section area of the steel core in the BRB.

ω and β consider the BRB overstrength caused by the steel strain hardening effect after yielding and the transfer of stress to the casing under compression, respectively [83]. The product of ω and β was taken as 1.5 as suggested by the BRB supplier.

2.3. BRB member design

The ultimate limit state (ULS) seismic load demand for each BRBGF at each level is shown in Fig. 1b. The load demand for the BRBGF specimens on Level 2 was 446 kN and the load demand for each BRB component was 301 kN considering the inclined angle $\alpha = 42°$. Commercial BRB products were used in this study with a characteristic yield capacity of 303 kN with assumed R_y. The steel core was a flat steel plate with Grade Q235 [78] and a cross section of 70 mm × 16 mm. The geometry information of the steel core is listed in Table 2. The steel core was covered by unbonding layers and then put into a 250 mm × 250 mm × 6 mm Grade Q235 steel casing. C30 concrete [84] was used to fill the space between the steel core and the steel casing. The BRBs were connected with the steel gusset plates by ϕ70 mm pins. All the steel gusset plates were designed according to NZS3404 [80] for tensile strength and Section E of AISC 360-16 [85] for stability. The effective length factor was chosen as 2.0 conservatively instead of 0.65 according to research from Tsai and Hsiao [86]. Table 3 lists the design strength of gusset plates. The steel plate thickness of the screwed connections was limited to 12 mm by the geometry of washers for STS, which caused the gusset plates were not strong enough as non-ductile members. Stiffeners were added on the gusset plates to reinforce them (Fig. 4).

Table 3: Gusset plate design strength (kN) and overstrength

Specimen	Gusset plate position	Compression	Tension	Overstrength
S-D	Top	569.4	1188.0	2.16
	Bottom	859.5	1188.0	3.27
S-S	Top	265.2	712.8	1.01
	Bottom	426.6	712.8	1.62

2.4. Glulam member and connection design

GL10 glulam [79] was used as the beams and columns. Because BRBs do not carry gravity loads after yielding, the glulam beams were designed with a full span of 8 m and the strength was checked according to NZS 3603 [79]. The beam and column cross sections were 585 mm × 315 mm and 315 mm × 315 mm, respectively, considering all possible load combinations in the prototype building. There was also a 10 mm gap between the beam and column to allow small joint rotation without causing significant crushing on the column.

In S-D, the dowelled connections consisted of ϕ12 mm Grade 300 [80] steel dowels and 20 mm-thick Grade 300 steel plates as shown in Fig. 3a. Each connection had two internal steel plates as gusset plates that had predrilled holes in diameter of 13 mm. The glulam members had two 22 mm-wide slots with a spacing of 125 mm and ϕ12 mm holes. The tolerance in the dowelled connections can cause slips and reduce the efficiency of the hybrid system. To minimize the tolerance in connections, all steel plates and timber members were manufactured by computer numerical control machines and the same diameter holes with the dowels were drilled in timber members as recommended by Eurocode

5 [54]. When installing the dowelled connections on site, the tip of each dowel was chamfered to fit the hole and prevent damaging the timber surface.

The characteristic strength $F_{v,Rk}$ of the dowelled connections was calculated using the model proposed by Fan [58] and Eq. (2)-Eq. (3) in Eurocode 5 [54] considering the effective number n_{ef} of dowels in each row. The top connection and bottom connections are at the same design strength hierarchy, so Fig. 3b shows the top connection layout as an example in which n_r and n_c are the row and column number of the dowel groups and the spacing follows the spacing requirements for dowels in Eurocode 5 [54]. The dowel groups in all connections aligned along the glulam member axes to reduce the moment caused by eccentricity and avoid timber splitting perpendicular to grain. The design strength values of connections listed in Table 4 were derived by considering the modification factor $k_{mod} = 1.1$ and the partial factor $\gamma_M = 1.25$ as per Eurocode 5 [54].

$$F_{V,Rk} = n_{ef} n_r (n_1 F_{V,Rk,1} + n_2 F_{V,Rk,2}) \tag{2}$$

with

$$F_{V,Rk,1} = min \begin{cases} f_{h,0,k} t_1 d \\ f_{h,0,k} t_1 d \left[\sqrt{2 + \frac{4M_{y,Rk}}{f_{h,0,k} d t_1^2}} - 1 \right] \\ 2.3 \sqrt{M_{y,Rk} f_{h,0,k} d} \end{cases} \tag{3a}$$

$$F_{V,Rk,2} = min \begin{cases} 0.5 f_{h,0,k} t_2 d \\ 2.3 \sqrt{M_{y,Rk} f_{h,0,k} d} \end{cases} \tag{3b}$$

$$f_{h,0,k} = 0.082(1 - 0.01d)\rho_k \tag{3c}$$

$$M_{y,Rk} = 0.3 f_{u,k} d^{2.6} \tag{3d}$$

$$n_{ef} = min \left[n_c, n_c^{0.9} \sqrt[4]{\frac{a_1}{13d}} \right] \tag{3e}$$

where, $F_{v,Rk,1}$ and $F_{v,Rk,2}$ are the load-carrying capacity per shear plane for steel plate as central member and outer member; $n_1 = 2$ and $n_2 = 2$ are the shear plane number of $F_{v,Rk,1}$ and $F_{v,Rk,2}$; $f_{h,0,k}$ is the characteristic embedment strength parallel to timber grain; $M_{y,Rk}$ is the yield moment of dowel; $t_1 = 83$ mm and $t_2 = 105$ mm are the side timber member and central timber member thickness, respectively; d is the diameter of fastener; $a_1 = 60$ mm is the spacing of fastener parallel to timber grain.

Table 4: Connection design strength (kN) and overstrength

	S-D ($n_r \times n_c$)	Overstrength	S-S ($n_r \times n_c$)	Overstrength
Top connection	619.9 (3 × 8)	1.59	619.0 (4 × 4)	1.59
Bottom connection on the beam side (BC-B)	332.2 (3 × 4)	1.70	309.5 (2 × 4)	1.58
Bottom connection on the column side (BC-C)	332.2 (3 × 4)	1.89	309.5 (2 × 4)	1.76

In S-S, the screwed connections consisted of $\phi 11 \times 300$ STS, washers and 12 mm-thick Grade 350 [80] steel plates as shown in Fig. 4a. Each connection had two steel side plates as gusset plates. The washers were used to accommodate the 45° inclined STS installation. Slotted holes for the washers were laser cut on the gusset plates following the washer product manual [82]. The geometry of the washers limited the gusset plate thickness to 12 mm, so stiffeners were welded on the gusset plates to increase the strength in compression as mentioned before. All STS were considered as tension-only STS (the darker colour STS under the force in Fig. 4a) as slotted holes were oversized and 4 mm longer than the washers according to the product manual (Fig. 14).

The characteristic strength $F_{ax,Rk}$ of the screwed connections was calculated as per Eq. (4)-Eq. (5) in Eurocode 5 [54] as axially loaded screws. The top and bottom connections in S-S were also designed at the same strength hierarchy. As shown in Fig. 4a, the horizontal component, R_{sx} governs the strength, i.e., the smaller value between the screw withdrawal strength ($F_{ax,45,Rk}$) and screw tensile strength ($f_{tens,k}$). Tests by Krenn and Schickhofer [69] showed that friction between the steel side plate and timber can also contribute to the connection strength due to the high vertical component, R_{sy}. However, European Technical Assessment document (ETA-11/0030) [81] does not allow to consider the benefits from friction. As the screwed connections in this hybrid system were not considered as ductile

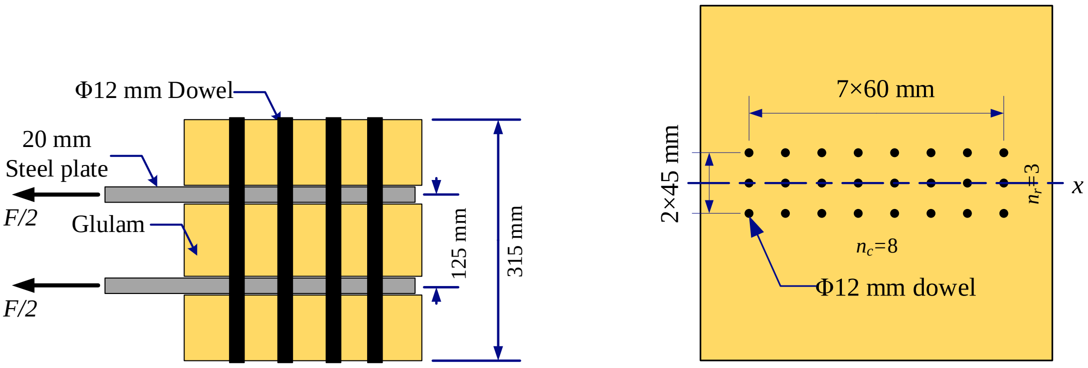

(a) Connection details

(b) Top connection layout

Figure 3: Dowelled connection

elements and should remain elastic, the friction contribution that could provide additional connection strength was not considered. The effective number of screws, n_{ef} was chosen to be 0.9 times the total screw number based on the tests by Krenn and Schickhofer [69]. The top connection and bottom connection layouts are shown in Fig. 4b and Fig. 4c, respectively. In the top connection, the STS that carried the loads in different directions were installed symmetrically along the centre of the top glulam beam, while in the bottom connections, the STS in different directions were installed staggeringly due to the space limit. The design strength of the screwed connections is listed in Table 4. The n_r and n_c are the row and column number of STS in tension at the load shown in Fig. 4.

$$F_{ax,Rk} = n_{ef} n_r R_{sx} \tag{4}$$

with

$$R_{sx} = min\left[F_{ax,45,Rk}, f_{tens,k}\right] \cos 45° \tag{5a}$$

$$F_{ax,45,Rk} = \frac{f_{ax,k} d l_{ef}}{1.2\cos^2 45° + \sin^2 45°} \left(\frac{\rho_k}{\rho_a}\right)^{0.8} \tag{5b}$$

$$n_{ef} = 0.9 n_c \tag{5c}$$

where, $F_{ax,45,Rk}$ is the characteristic withdrawal capacity of STS; $f_{tens,k}$ is the tensile strength of STS; $f_{ax,k}$ is the characteristic withdrawal parameter; $l_{ef} = 249\,\mathrm{mm}$ is the penetration length of the threaded part of STS; $\rho_a = 350\,\mathrm{kg/m^3}$.

3. Test programme

3.1. Test matrix and loading protocol

Table 5 lists the test matrix including the frame tests and the BRB component tests. The drift ratios in Table 5 were the maximum drift ratios achieved in each test.

In the frame tests, glulam column bases and the mid-span shear connection of the bottom glulam beams were anchored to the strong floor by steel brackets and the dowelled connections so the specimens were fixed horizontally and vertically at the bases in the frame plane as shown in Fig. 5. The top glulam beam was connected to a steel loading beam that was also connected to an 800 kN actuator mounted on the reaction wall. The out-of-plane movement was restrained by two actuators at the positions of the columns, so the specimens were considered to be rigid out of plane.

The frame tests followed ISO 16670 [87] loading protocol shown in Fig. 6 and the positive direction was the north (N) direction in Fig. 5. The specimens were loaded with drift ratios of 0.03%, 0.06%, 0.13%, 0.19%, 0.25%, 0.5%, 1.0%, 1.5% and 2.0%, and the loading rate was between 8 mm/min and 12 mm/min. The tests T1 and T3

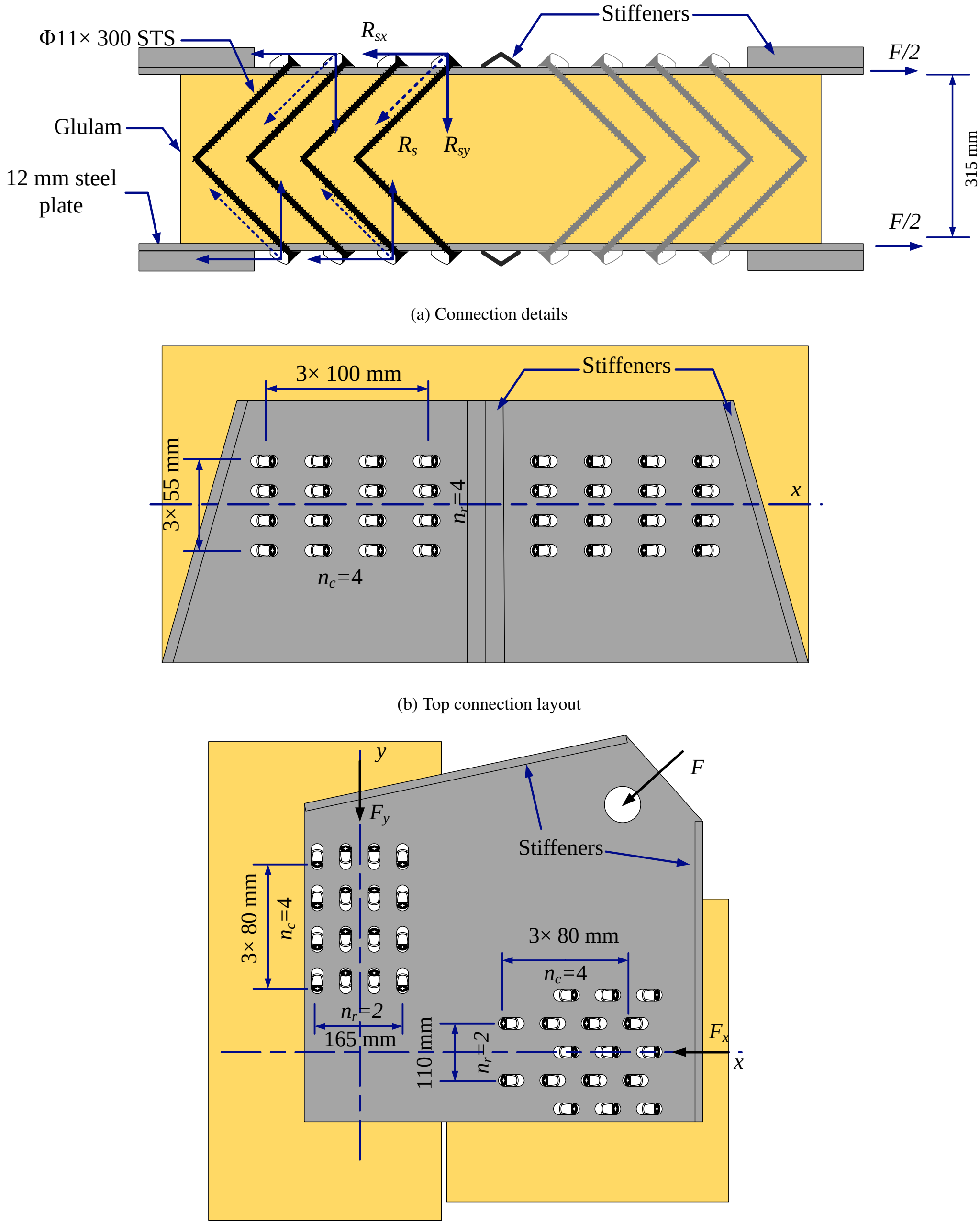

(a) Connection details

(b) Top connection layout

(c) Bottom connection layout

Figure 4: Screwed connection

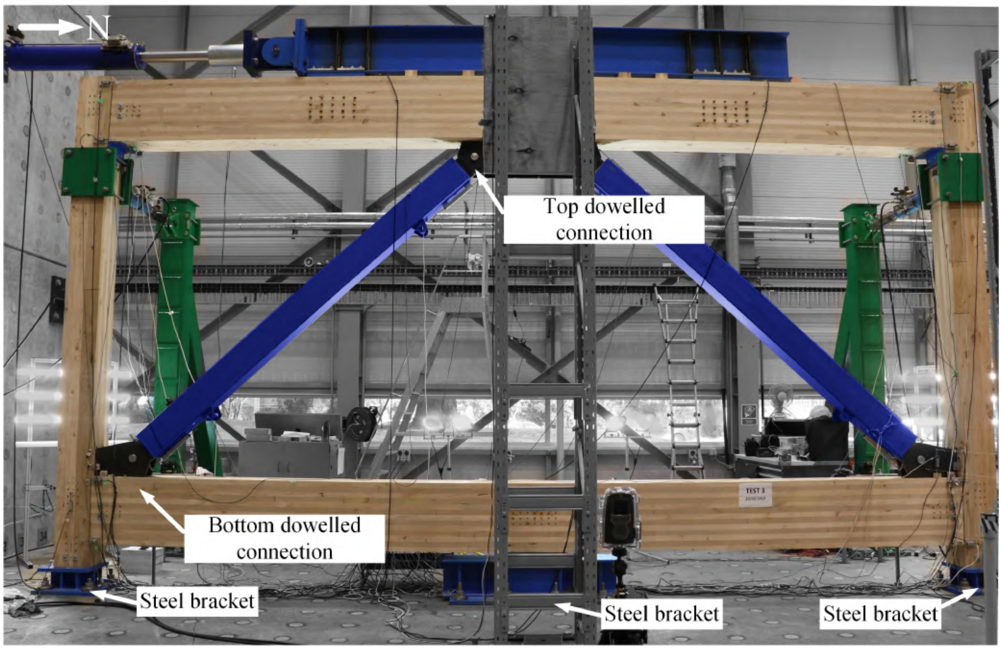

(a) S-D with the dowelled connections

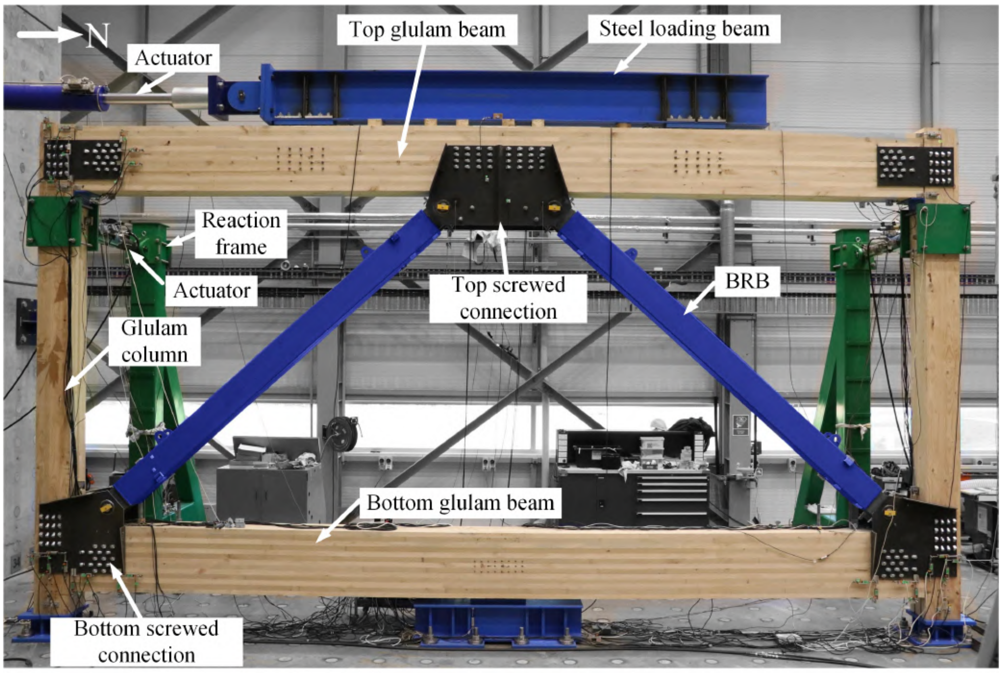

(b) S-S with the screwed connections

Figure 5: Test specimens

Table 5: Test matrix

Test phase	Specimen	Test No.	Objective	Drift ratio
I: frame tests	S-D	T1: BRBGF cyclic test	Evaluate ULS	1.5%
		T2: bare frame test	Evaluate the bare frame's deformation capacity	2.0%
	S-S	T3: BRBGF cyclic test	Evaluate ULS	1.5%
		T4: bare frame test	Evaluate the bare frame's deformation capacity	2.0%
II: BRB component tests	BRB-D	T5: cyclic test	Evaluate the BRB residual performance	2.0%*
	BRB-S	T6: cyclic test	Evaluate the BRB residual performance	
	BRB-U	T7: cyclic test	Evaluate the BRB property	

* BRBs were loaded to the displacement they would achieve when the BRBGF was loaded to this drift ratio

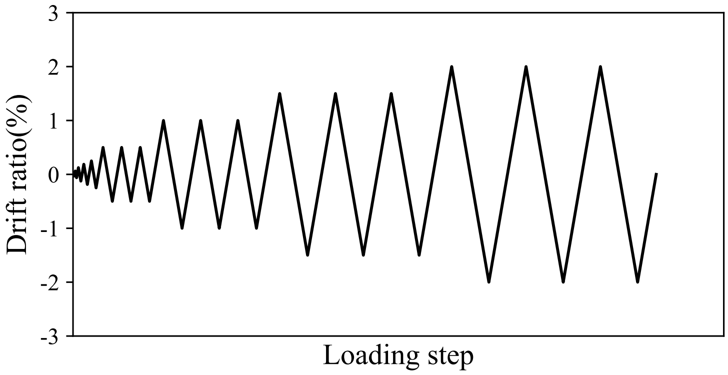

Figure 6: ISO 16670 loading protocol

were finished at 1.5% drift ratio when maximum capacity of the actuator was reached, while the tests T2 and T4 were finished at 2.0% drift ratio.

As the BRBs are designed to govern the hybrid system performance, it is important to ensure the BRB design parameters such as f_{ys}, ω and β are consistent with the design specifications. In the BRBGF tests, two BRBs carried the lateral load together and the force distribution between two BRBs could not be measured accurately. In this regard, three BRB component tests were also conducted under uniaxial cyclic loading (Fig. 7). Two BRBs (BRB-D and BRB-S) were taken from the specimens S-D and S-S, respectively, after the frame tests. One BRB (BRB-U) was unused but manufactured in the same batch as the BRBs installed in the frames. The loading protocol followed AISC 341-16 [48] and the results of three BRB components were compared to check the brace performance consistency.

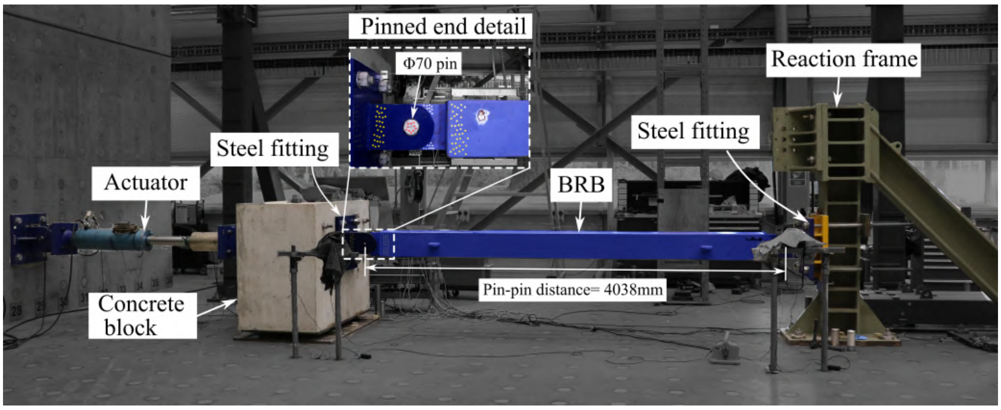

Figure 7: BRB component test setup

3.2. Measurements

The locations of measuring devices are shown in Fig. 8. A load cell was used to measure the load in the actuator; inclinometers (Is) were installed at beam-column connections to measure the connection rotation (Fig. 8b); string potentiometers (SPs) were installed at the top glulam beam and bottom glulam beam to measure the frames' inter-storey drift (Fig. 8c); linear-motion potentiometers (LPs) were installed on both ends of BRBs' casing to measure the BRBs' elongating and shortening between the casing and the steel core (Fig. 8d). BRBs' tension and compression deformation was the sum of the deformation on both ends.

In S-D, gusset plates were inserted into glulam; in S-S, glulam surfaces were covered by the gusset plates. It is challenging to accurately measure the connection movement with traditional instruments. Therefore, Particle Tracking Technology (PTT) [88] was adopted in this study. PTT was recently used in structural timber tests to capture crack growth of exposed timber surfaces in dowelled connections and also compute the resulting displacement field [89]. The PTT measurements are shown in Fig. 9 by taking the southern bottom connection of S-D as an example. Small particles were attached to the surface of glulam members and gusset plates, as shown in Fig. 9a. Digital cameras were used to take photos at each load step and track the movement of the particles. All photos were processed by Streams [88] to obtain the displacement of particles and their corresponding displacement field. In this manner, the movement of each visible point in the photos can be exported from the displacement field. As all gusset plates and glulam members' elastic deformation was negligible when compared to the connection deformation, the gusset plates and glulam members in the connection zone could be assumed to have rigid body motion. As shown in Fig. 9a, the movement of points A and B on the gusset plate and point C' at the centroid of a dowel on the glulam surface was directly tracked by PTT. The movement of point C at the centroid of the dowel on the gusset plate plane was derived by the movement of points A and B in the triangle ΔABC as point C was not visible. The relative movement of point C and point C' defined the dowel deformation as shown in Fig. 9b. In this manner, each connection's movement could be evaluated. For S-S, similar process was conducted by PTT to track the movement of washers and glulam members. The relative movement between washers and glulam members was used to estimate the STS deformation.

4. Experimental results

4.1. S-D and S-S response

In S-D, a small number of dowels experienced minor bending deformations and some holes in the gusset plates had minor crushing under the dowel bearing loads in both the top and bottom connections. Fig. 10 shows an example at the bottom connections. In S-S, slight bending deformation at the edge of the gusset plates was observed in the top connection as shown in Fig. 11 when the load exceeded the design load. STS were removed from the screwed connections and no visible damage was observed. Both specimens had residual drifts due to the residual deformation of the BRBs (Fig. 12).

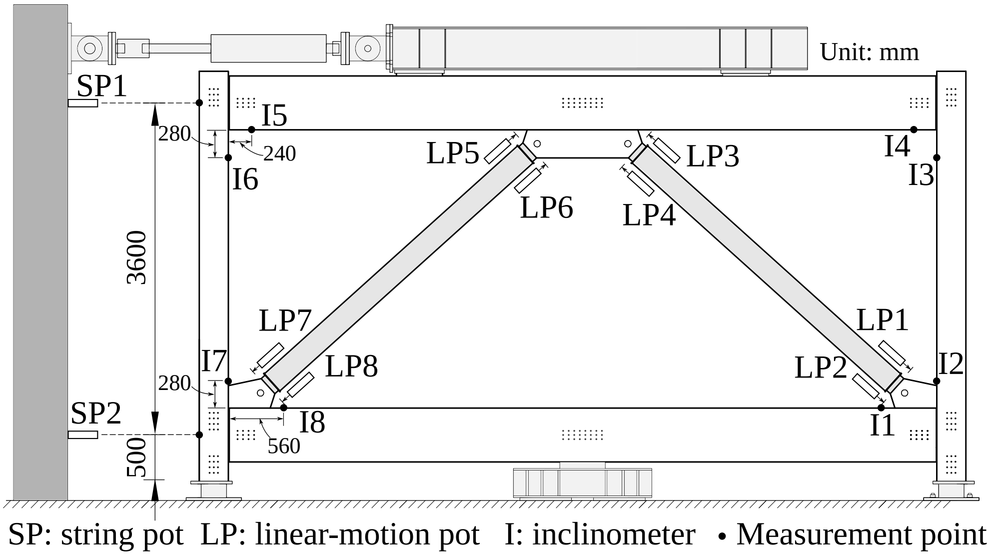

(a) Instrument layout

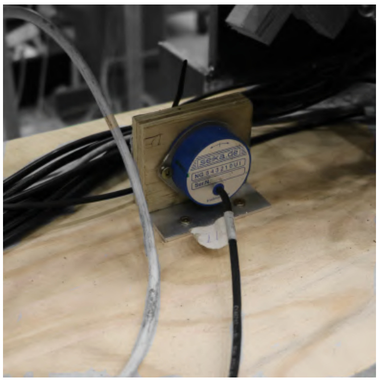

(b) Inclinometer

(c) Spring potentiometer

(d) Linear-motion potentiometer

Figure 8: Instruments

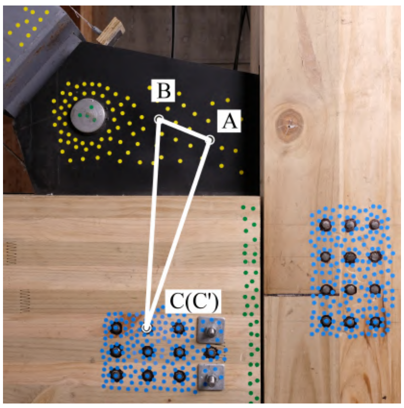

(a) Particles on the connection

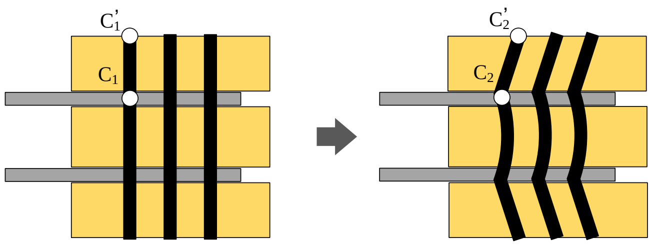

(b) Connection movement calculation process

Figure 9: PTT measurements

(a) Dowels' bending

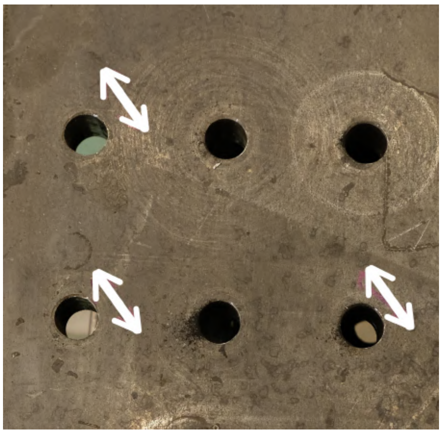

(b) Oval holes in the gusset plate

Figure 10: Damage of S-D

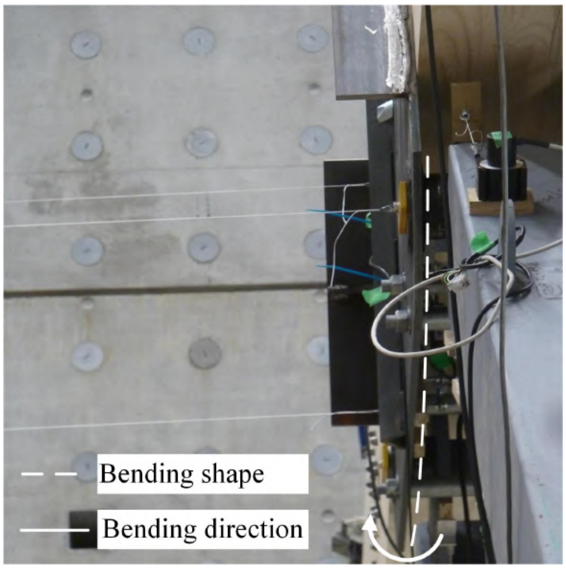

Figure 11: Gusset plate bending deformation in S-S

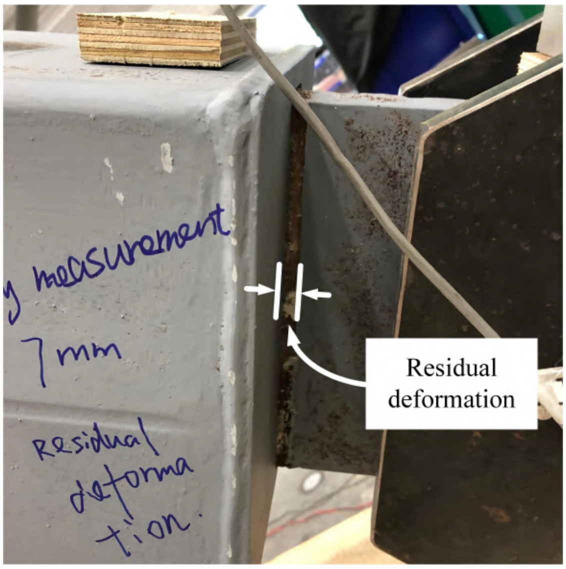

Figure 12: BRB's residual deformation

4.2. Load-drift hysteresis curves of BRBGF specimens

In tests T1 and T3, both specimens were loaded to 1.5% drift ratio. The hysteresis curves and their backbone curves are shown in Fig. 13. The drift was the inter-storey drift by removing the displacement of SP2 from that of SP1 shown in Fig. 8a.

Fig. 13a shows that S-D experienced three stages: initial slip stage, elastic stage and post-yield stage. First, the initial stiffness was low when the drift was within ±4.5 mm. The initial slips were primarily attributable to three factors: (1) the holes on the BRBs for the pinned connections were manufactured by plasma cutting and were up to 2 mm oversized; (2) holes in the gusset plates for the dowels were 1 mm oversized for installation convenience; (3) the stiffness of the surface layers of the dowel holes was lower than that of the surrounding bulk wood [90]. After the initial slip stage, BRBs were fully engaged in carrying the loads and the system became very stiff until BRB yielding. The stiffness of S-D decreased gradually when the BRBs started to yield. The maximum residual drift ratio was 0.9% (32.1 mm drift).

Fig. 13b shows that S-S had similar performance with S-D. The main difference was that S-S had less initial slips, which were within ±2.0 mm. This was because the inclined STS engaged in the axial direction were tight-fit and stiffer when compared with laterally loaded dowels with similar diameters [69]. However, the unloading process showed that the slips gradually increased at around zero load. The main reason for the increasing slips might be that the slotted holes were oversized (Fig. 14) and the beam-column connection rotation caused the slips of washers in the slotted holes. Some washers became loose and gaps were observed between washers and screw heads during the testing (Fig. 15). These STS were not in tension until the washers contacted the gusset plates tightly again. The maximum residual drift ratio was 0.9% (31.5 mm drift).

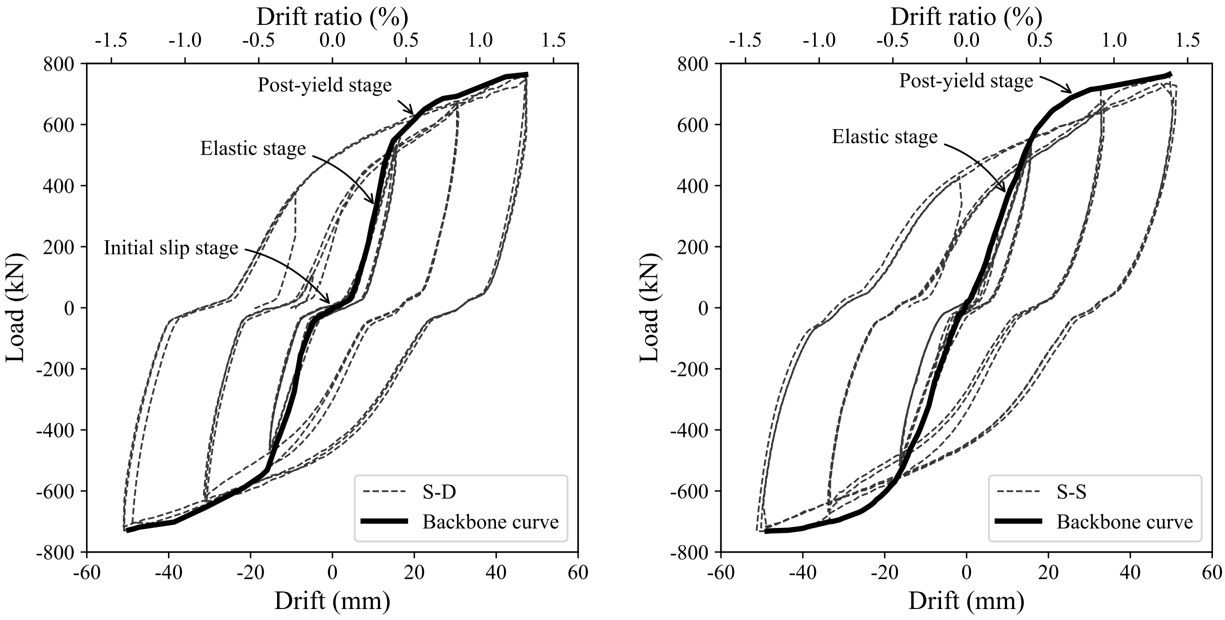

(a) S-D test T1 hysteresis curve and backbone curve

(b) S-S test T3 hysteresis curve and backbone curve

Figure 13: Hysteresis curves and backbone curves

The maximum strength of both specimens is listed in Table 6. Popovski et al. [91] conducted shake table tests on 130 mm × 152 mm diagonal glulam braces with bolted connections and the maximum strength was 79.8 kN. Xiong et al. [53] tested two 4110 mm wide and 2740 mm high glulam frames with inverted-V glulam braces (cross section 135 mm × 105 mm) and bolted connections under cyclic loading. The maximum strength was only 129.5 kN and 128.1 kN, respectively. In this study, the tested two BRBGFs had much higher capacity by integrating BRBs, thus this hybrid system has the potential to be applied in mid-rise buildings as LFRS.

The serviceability limit state (SLS) stiffness k_{SLS} was defined as the secant stiffness at 1/300 drift ratio [92, 93]. The backbone curves had two well-defined linear parts, and their tangent stiffness values were defined as elastic stiffness k_1 and plastic stiffness k_2 to calculate the yield strength F_y and yield drift δ_y as per EN12512 [94]. The three types of stiffness values are listed in Table 6. Although S-D had larger initial slips, it achieved higher k_1 than S-S when the dowels were fully engaged. Because of this, k_{SLS} of S-S was only slightly higher than k_{SLS} of S-D. It illustrates that when the lateral load was lower than the SLS level, S-S would be more efficient and had less drift when compared to S-D, while S-D and S-S would have similar drift when the lateral load was higher than the SLS level. Furthermore, the tangent stiffness of the backbone curves is shown in Fig. 16. The stiffness decreased significantly after BRB yielding, which was quite different from the BRBF with moment-resisting connections. For example, the test results from Jia et al. [95] showed BRB composite frame's tangent stiffness decreased gradually but still kept more than 20% of initial stiffness until failure. The stiffness results illustrates that the beam-column connections were closer to pinned connections, which could help to reduce the frame action and avoid early failure of the frames [96].

Table 6: Strength, stiffness and ductility properties of two frame specimens

Property	S-D			S-S		
	P*	N**	Mean	P	N	Mean
Maximum strength F_{max} (kN)	763.5	729.9	746.7	764.4	731.8	748.1
Maximum drift δ_{max} (mm)	47.4	51.0	49.2	51.3	51.3	51.3
Yield strength F_y (kN) (CEN)	595.6	539.6	567.6	626.5	593.1	609.8
Yield drift δ_y (mm) (CEN)	15.5	14.7	15.1	16.9	16.2	16.6
SLS stiffness k_{SLS} (kN/mm)	32.0	35.4	33.7	34.7	35.2	35.0
Elastic stiffness k_1 (kN/mm)	55.2	53.2	54.2	38.7	40.4	39.5
Plastic stiffness k_2 (kN/mm)	6.0	5.6	5.8	4.5	5.1	4.8
Initial slip δ_s (mm)	4.7	4.5	4.6	0.7	1.6	1.2
Ductility factor μ (CEN)	3.1	3.5	3.3	3.0	3.1	3.1

* P = positive drift direction
** N = negative drift direction

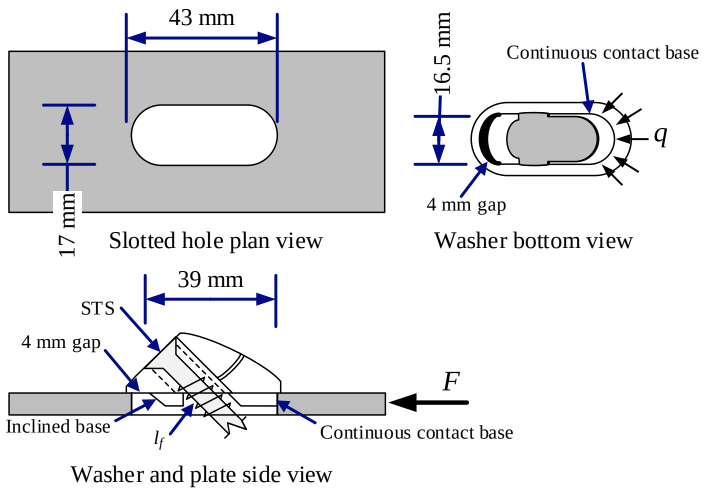

Figure 14: Oversized slotted holes

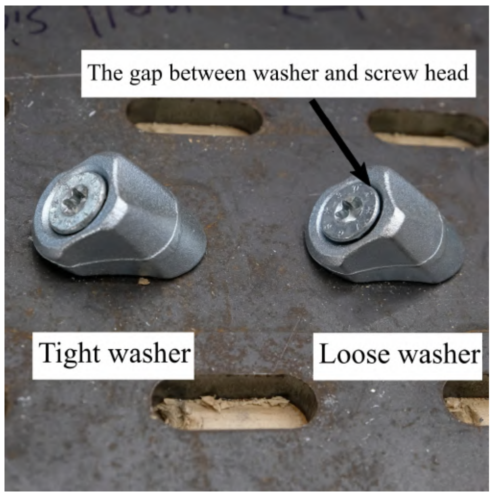

Figure 15: Tight and loose washers

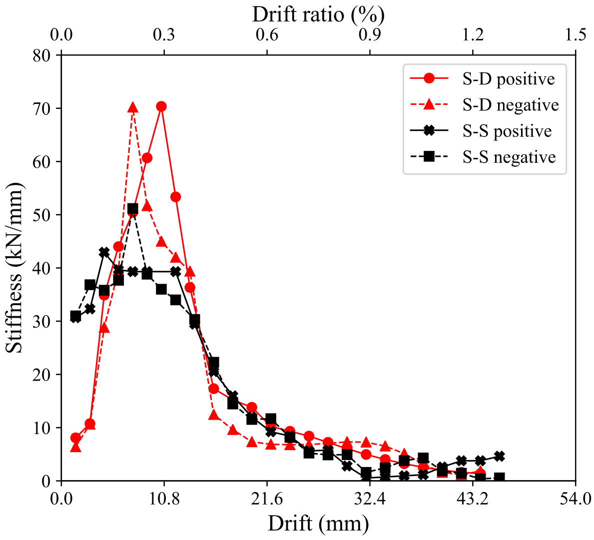

Figure 16: Stiffness degradation of backbone curves

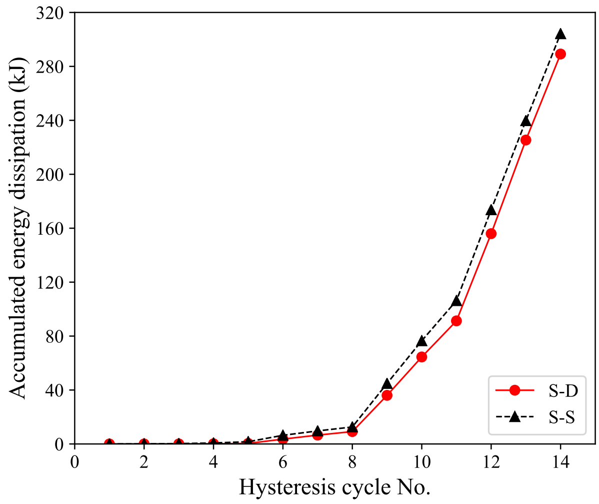

Figure 17: Energy dissipation capacity of two specimens

4.3. Energy dissipation and ductility

The ductility factor μ is normally defined by Eq. (6), which is the ratio between the ultimate displacement δ_u and the yield displacement δ_y. δ_u is normally defined as the displacement at which the load drops to 80% of the peak load. In the BRBGF testing, since no obvious failure or load decrease was observed, $\delta_u = \delta_{max}$ was used to calculate μ and δ_{max} is the maximum drift at the peak load. There are different methods to define δ_y. The CEN method in EN12512 [94] obtains reasonable δ_y for systems with an elevated initial stiffness [97], so it was used in this study to calculate the δ_y and μ as listed in Table 6. The EEEP method in EN2126 [98] tends to overestimate yield strength and may lead to a misclassification of systems [97]. Nevertheless, μ results based on EEEP method were still calculated to compare with test results of conventionally braced timber frame from Xiong et al. [53]. Based on EEEP method, the ductility factor of BRBGFs was 2.3-2.8, which was more than double when compared to that of the conventionally braced timber frames (1.0-1.2). It should also be noted that the derived ductility from this study was the minimum ductility the hybrid system could achieve as the post-peak ultimate displacement was not reached.

$$\mu = \frac{\delta_u}{\delta_y} \tag{6}$$

Fig. 17 shows that accumulated energy dissipation of two frame specimens. The energy dissipation started to increase significantly after BRB yielding at cycle 9. In total, S-D and S-S dissipated 289 kJ and 304 kJ in 14 cycles, respectively. The full hysteresis curves and accumulated energy dissipation showed good energy dissipation capacity.

4.4. BRB component tests

The design storey drift was 23 mm that was the product of μ and deflection calculated by equivalent static method as per NZS 1170.5 [76]. Because 23 mm was smaller than the minimum design storey drift ratio for BRBF (1% , i.e. 36 mm) as per AISC 341-16 [48], 1% was set as the design storey drift ratio for BRB component tests and all BRBs were loaded to the displacement corresponding to two times the design storey drift ratio, which was 54 mm considering the inclined angle $\alpha = 42°$ in the frame. Fig. 18 shows the hysteresis curves of the three BRBs and the maximum displacement was slightly smaller than 54 mm as the slips at pin holes on both ends of BRBs have been removed. Their strength at the similar displacements was compared in Table 7. The BRB strength properties were consistent with a coefficient of variation (COV) less than 5%. Since the BRBs were stronger than the specification, to figure out the reasons, coupon tests were conducted by using the offcut from the steel core of BRBs after the BRB component tests (Fig. 19). The actual yield strength from coupon tests $f_{ys,act}$ was 294 MPa with $R_y = 1.25$, which was slightly higher than the specification (1.15) in AISC 341-16 [48]. The actual yield strength $F_{y,BRB-U}$ and yield displacement $\delta_{y,BRB-U}$ of BRB-U were 329.3 kN and 4.6 mm calculated by Eq. (7) and Eq. (8), respectively, based on research from Tsai and Hsiao [86] and data in Table 2. The accumulated ductility of BRB-U was 321, which met the minimum requirement of 200 in AISC 341-16 [48]. However, ω and β were 1.86 and 1.18, respectively. $\omega\beta = 2.19$ was 46% higher than the specification (1.5). The significant overstrength caused that the actuator reached its loading capacity before two BRBF specimens were loaded to 2.0% drift ratio. The cut open of steel core (Fig. 20) shows that the unbonding materials stuck on the steel core tightly with limited gaps. The high overstrength might be caused by the inappropriate unbonding between the steel core and the concrete grout. BRB quality control is essential to ensure that the BRB's performance is consistent with the specifications used in the design [99].

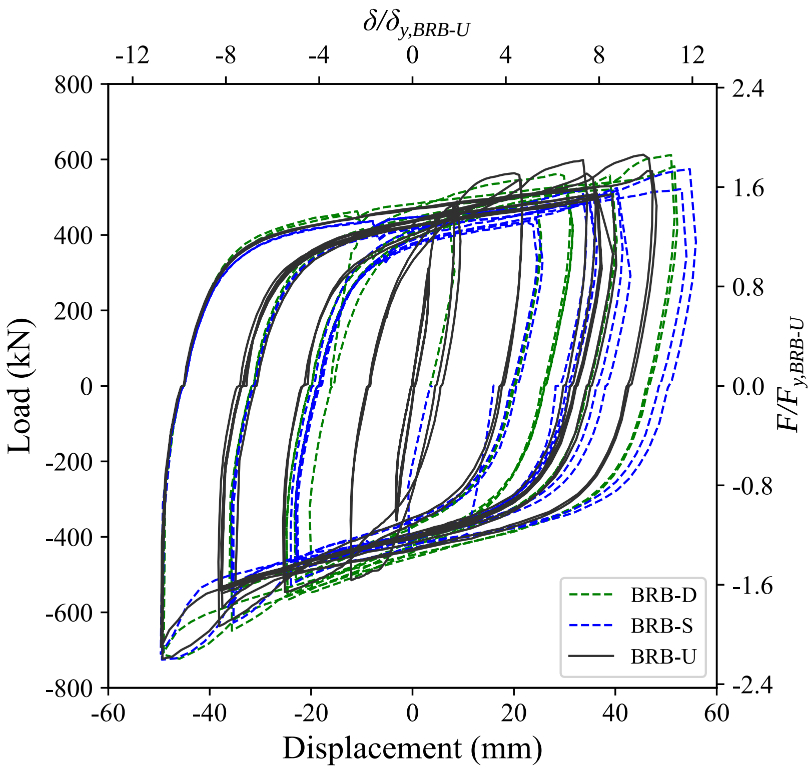

Figure 18: BRB hysteresis curves

Table 7: BRB strength comparison

Specimen	Displacement (mm)		Strength (kN)	
	Tension	Compression	Tension	Compression
BRB-D	49.3	49.3	568.3	709.0
BRB-S	49.6	49.6	563.1	710.0
BRB-U	48.1	49.6	612.7	723.1
Maximum of COV			4.7%	1.1%

$$F_{y,BRB-U} = f_{ys,act} A_c \tag{7}$$

$$\delta_{y,BRB-U} = F_{y,BRB-U} / K_{eff} \tag{8}$$

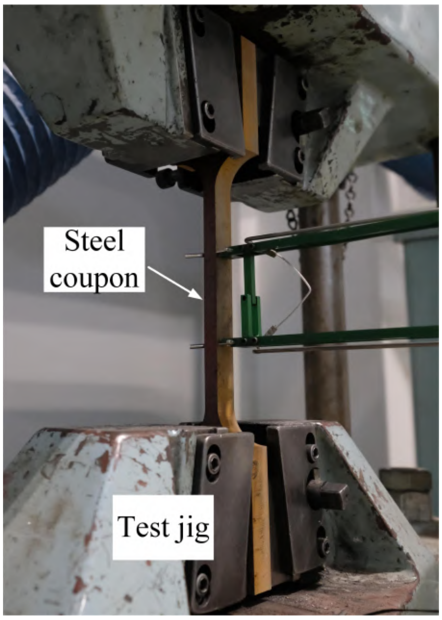

Figure 19: Steel coupon test

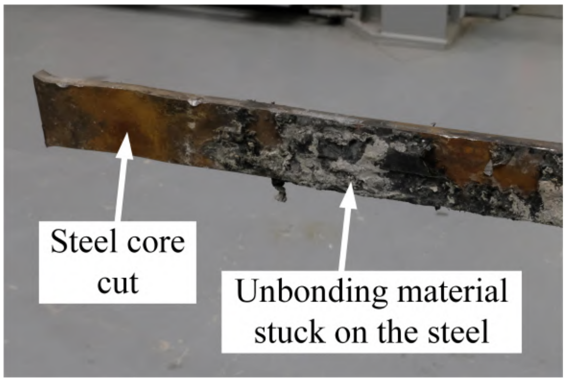

Figure 20: Steel core cut open

with

$$K_{eff} = E_s A_c A_{tr} A_e / (A_c A_{tr} l_e + A_c A_e l_{tr} + A_{tr} A_e l_c) \tag{9}$$

4.5. Connection behaviour

4.5.1. Connection rotation stiffness

In test T1 and T3, the rotation of columns was measured by inclinometers. Two columns in each specimen had similar rotation response, so the results of the southern column in each specimen are shown in Fig. 21 as examples. The results illustrated that the top and bottom of columns had co-directional rotation, so the columns carried minimum moments. The reason that the top of the column had slightly larger rotation than the bottom of the column was that the column bottom bore against the steel brackets and carried small moments. Therefore, the beam-column connections can be considered as pinned-connections approximately.

In test T2 and T4, two bare frames (S-D and S-S without BRBs) were tested to 2.0% drift ratio. The hysteresis curves are shown in Fig. 22. The bare frames carried less than 35 kN lateral load at 1.5% drift ratio, so it was found that the bare frames' contribution to the total capacity of the hybrid system was less than 5% at this drift ratio. Tests of BRBs with moment resisting frames (MRF) showed that the MRF could carry 30% to 50% of the total lateral load [20]. Therefore, the beam-column connections behaved as pinned connections approximately, which also matched with the BRBGF behaviour discussed above.

The bare frame tests showed that the beam-column connections had enough flexibility to accommodate 2.0% drift ratio and the BRB component tests showed that the deformation of the BRBs could accommodate 2.0% drift ratio without significant loss of the capacity. Consequently, it would be possible for the BRBGF specimens to achieve a minimum ductility of 4.2 according to CEN method at 2.0% drift ratio if the overstrength of the BRBs could be well controlled.

4.5.2. Top connection behaviour

The top connections' relative movement between the gusset plate and glulam members was well captured by PTT. Fig. 23 shows the layout of the top connection in S-D and S-S. Table 8 lists the connection movement magnitudes in the x and y direction. The connection movement was very small and within ± 3 *mm*. The load-displacement curves of the top connections are also shown in Fig. 24. The load was estimated to be 95% of the actuator's load according to the bare frame test results and the displacement was the connection movement in the x direction. The connection

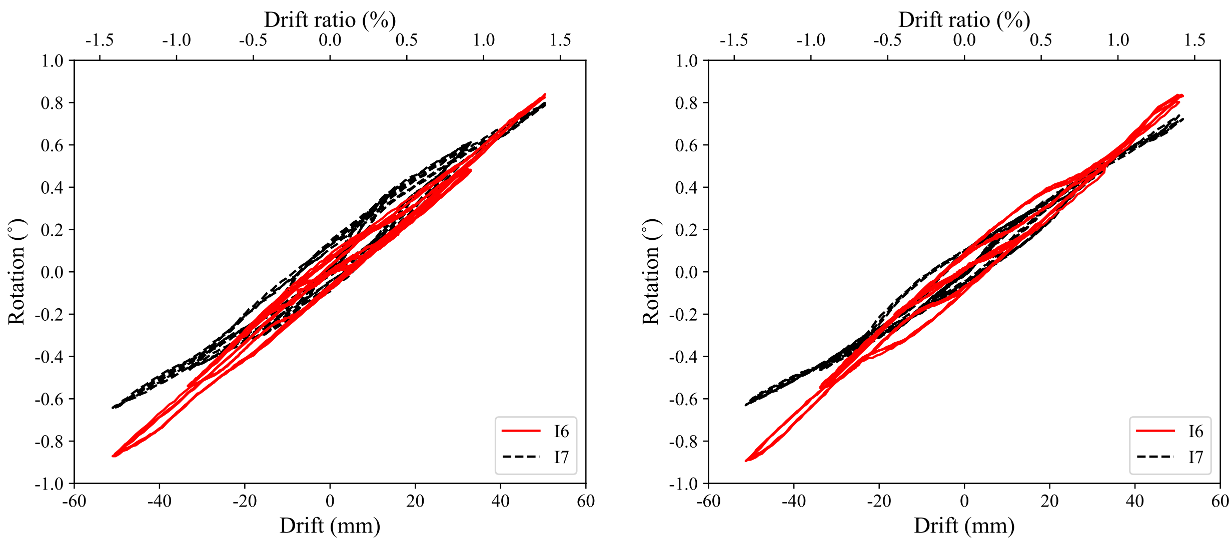

(a) S-D

(b) S-S

Figure 21: The column rotation measured by inclinometers

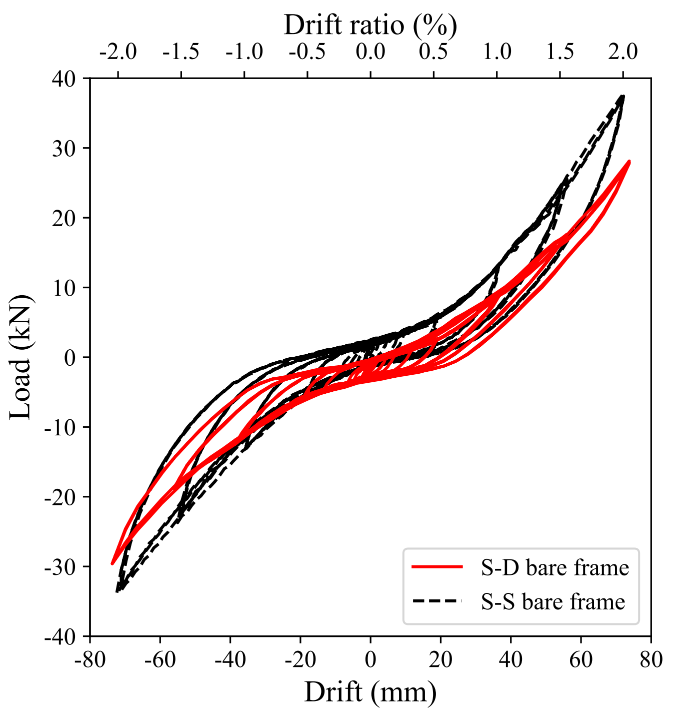

Figure 22: Bare frame hysteresis curves

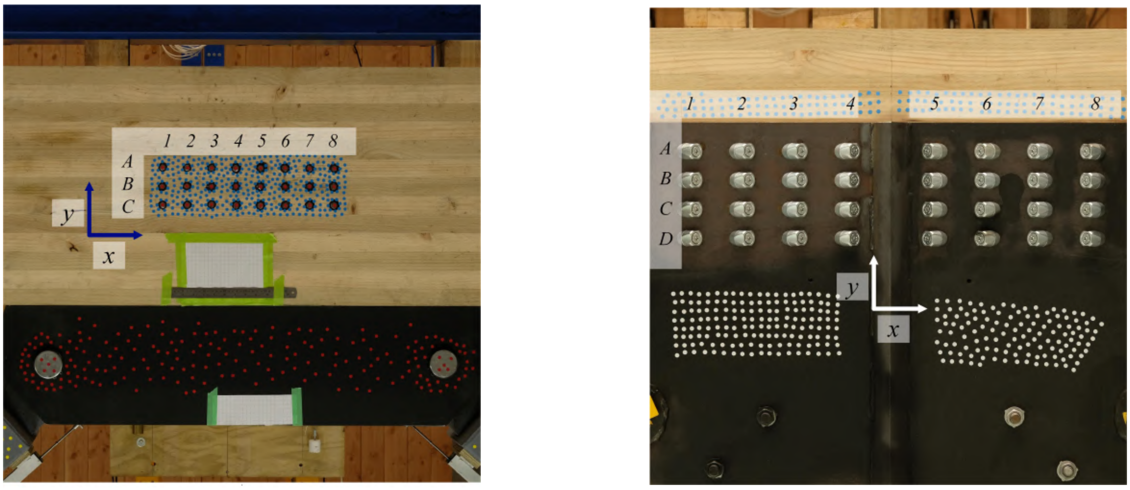

(a) Dowelled connection (b) Screwed connection

Figure 23: Top connection details in S-D and S-S

design strength, the SLS stiffness (k_{ser}) and the ULS stiffness (k_u) were also plotted. The predicted and actual k_{ser} and k_u are listed in Table 9. In S-D, the predictions of k_{ser} and k_u followed Eq. (10) and Eq. (11) as per Eurocode 5 [54]; in S-S, the prediction of k_u followed Eq. (11) as well, while the prediction of k_{ser} followed Eq. (12) from Tomasi et al. [67] without considering the frictional effect ($\mu_f = 0.0$). The actual stiffness was derived from the backbone curves. The actual k_{ser} was defined as the slope of the line between $0.1F_{max}$ and $0.4F_{max}$ according to EN12512 [94] and the actual k_u was defined as the secant stiffness at 70% of maximum strength during the tests [100]. The actual stiffness values listed in Table 9 represent the average value of positive and negative backbone curves.

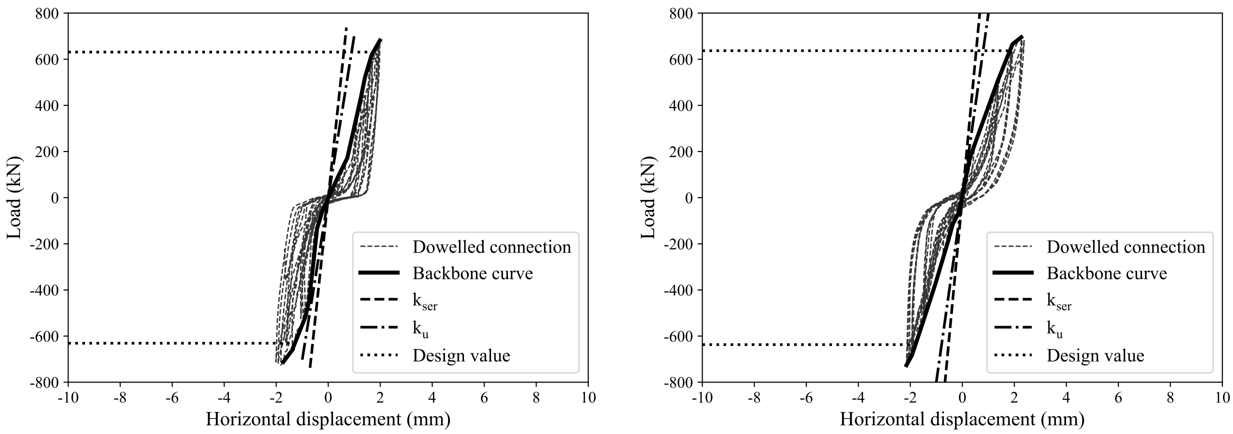

(a) S-D (b) S-S

Figure 24: Load-displacement relationships in the top connections of S-D and S-S

$$k_{ser} = 2\rho_m^{1.5}\frac{d}{23} \tag{10}$$

$$k_u = \frac{2}{3}k_{ser} \tag{11}$$

$$k_{ser} = k_\perp \sin\theta(\sin\theta - \mu_f\cos\theta) + k_\parallel \cos\theta(\cos\theta + \mu_f \sin\theta) \tag{12}$$

Table 8: Top connection movement

Connection	Magnitude in x direction (mm)	Magnitude in y direction (mm)
Dowelled connection	+2.2/-2.6	+0.7/-1.1
Screwed connection	+2.5/-2.2	+1.1/-2.9

Table 9: Top connection stiffness

Stiffness (kN/mm)	S-D		S-S	
	k_{ser}	k_u	k_{ser}	k_u
Predicted value	1007	672	1198	798
Actual value	502	473	371	366

with

$$k_{\perp} = 2\rho_m^{1.5}\frac{d_{ef}}{23} \tag{13a}$$

$$k_{\parallel} = 25dl_{ef} \tag{13b}$$

where, k_{ser} is the SLS stiffness; ρ_m is the mean value of timber density; d is the diameter of fasteners; d_{ef} is the effective diameter of STS; $k_{\perp}$ is the SLS stiffness perpendicular to STS axis; $k_{\parallel}$ is the SLS stiffness parallel to STS axis as per ETA-11/0030 [81]; θ is the angle between STS axis and timber grain; μ_f is the friction coefficient at timber-steel interface.

For the dowelled connection, Fig. 24a shows that the dowelled connection had lower initial stiffness but increased significantly after the low initial stiffness stage. Actual stiffness values in Table 9 show that the stiffness of the dowelled connection did not decrease significantly (502 kN/mm vs. 473 kN/mm with 6% difference) at the design strength level, which meant that the connection had enough capacity without obvious stiffness degradation. However, the connection's actual stiffness was much lower than the predicted value, which matched the conclusions with research from Sandhaas et al. [63]. One reason was that Eq. (10) was highly simplified and only considered the influence of density and dowel diameters. More parameters such as number of dowels [101] and slenderness of dowels [64] can affect the connection stiffness. Another reason could be that using 2 as the modification factor in Eq. (10) for timber-steel interface is not appropriate [102]. The hole deformation was observed during the tests as shown in Fig. 10b, which illustrated that the steel interface was not fully rigid. For connections with the test layouts, it is suggested to take modification factor as 1 instead of 2 to compromise those factors that are not considered in Eurocode 5 [54], which was also recommended by Wang et al. [103]. To estimate the stiffness more accurately for different layouts, the stiffness of connections requires further investigation such as the alternative design method based on the beam-on-foundation modelling. At the design load level, the stiffness started to round off, thus the predictions provided a reasonable estimation for strength but over predicted the stiffness of the dowelled connections.

For the screwed connection, Fig. 24b shows that the backbone curve was almost linear and Table 9 shows that the stiffness of the screwed connection almost kept the same at the design strength level (371 kN/mm vs. 366 kN/mm with 1% difference). The actual stiffness was lower than the one of the dowelled connection and much lower than the predictions. Previous research in timber-timber connections showed that k_{ser} of 45° inclined STS could be roughly 12 times that of laterally loaded STS installed with 90° angles [104]. Although the Eurocode 5 [54] could over predict $k_{\perp}$, which was similar with the dowelled connections, $k_{\perp}$ should be much smaller than $k_{\parallel}$ [74]. Thus, the main reasons for the over-predictions of Eq. (12) should be from $k_{\parallel}$. The over-prediction of $k_{\parallel}$ was because that Eq. (13b) was also highly simplified and did not consider the flexibility of STS [73] and timber density. In addition, it is not appropriate to consider that $k_{\parallel}$ is proportional to the penetration length l_{ef}, especially for long STS [105]. Another reason could be that the STS had free length (l_f in Fig. 14) in the steel plate and the free length had elastic bending deformation under the lateral loads. Because STS are flexible fasteners, the bending deformation can be comparable to the STS embedment and withdrawal movement. This was also the reason that the stiffness of the screwed connections was lower than that of the dowelled connections after dowels were fully engaged. The stiffness of the screwed connections requires further investigation as well. At the design strength level, the stiffness did not round off, which showed that the strength prediction in Eurocode 5 [54] was conservative since the additional contribution from friction was not considered. Previous research showed that the friction contribution could increase the strength by at least 25% [69]. As a consequence, the predictions provided a conservative estimation for strength but over predicted the stiffness of the screwed connections.

Although the stiffness predicted by standards could overestimated the stiffness significantly, the connections protected by overstrength were still strong and stiff enough to allow BRBs to yield and dissipate energy with small connection deformation. Therefore, the capacity design approach is not only important to protect the non-ductile members, but also to ensure enough stiffness of connections. The connection test results will be used to calibrate numerical models and the influence of connection stiffness will be further discussed based on the modelling results, which is out of the scope of this paper.

4.5.3. Bottom connection behaviour

The bottom connections' relative movement between the gusset plates and glulam members was captured by PTT as well and Fig. 25 shows the layout of the southern bottom connection in S-D and S-S as examples. However, different with the top connections, the forces transferred from BRBs into the bottom connections could not be estimated accurately. The reason was that the BRB under compression carried more load than the one under tension caused by the compression strength adjustment factor β. β varied at different drift level and thus changed the force distribution between two BRBs under cyclic loading. The bottom connections on the beam side and column side are denoted as BC-B and BC-C, respectively as shown in Fig. 25 and the relative moment of bottom connections are listed in Table 10. Table 10 shows that similar magnitudes for bottom connections were observed with the top connections and thus the bottom connections should have similar performance with the top connections. However, it is noticed that BC-C in both S-D and S-S had larger movement in the direction perpendicular to timber grain when compared with the top connections. This illustrated that part of horizontal forces transferred to the columns. The extra horizontal force could cause extra slips of washers in the screwed connections, which could increase the slips at unloading stage. Some lateral STS installed 90° to the timber and gusset plate surfaces are recommended to resist the horizontal forces in BC-C and minimize the slips.

(a) Dowelled connection (b) Screwed connection

Figure 25: Bottom connection details in S-D and S-S

Table 10: Bottom connection movement

Connection	Position	Magnitude in x direction (mm)	Magnitude in y direction (mm)
Dowelled connection	BC-B	+1.4/-2.0	+0.9/-0.6
	BC-C	+1.8/-1.5	+1.8/-2.5
Screwed connection	BC-B	+1.5/-1.7	+1.1/-1.2
	BC-C	+3.2/-3.0	+2.3/-1.8

5. Conclusions

The cyclic performance of two full-scale 8 m wide and 3.6 m high BRB glulam frames (BRBGFs) with two different connection options (the dowelled and screwed connections) were experimentally studied in this paper. The capacity design approach was used to design the hybrid system with BRBs specified as ductile elements and glulam members and connections specified as non-ductile elements. The dowelled and screwed connections were used to connect glulam frames with BRBs. The primary findings are listed as follows:

- The hybrid frames had much higher load-carrying capacity when compared with previous test results from conventionally braced timber frames. The capacity design approach proved to work well for this hybrid frame system. The BRBs performed as ductile elements and provided enhanced ductility and energy dissipation for the frame. The ductility was more than double when compared with that of conventionally braced timber frames. Non-ductile glulam members and connections were well protected with minor damage after the load exceeded the design value.
- The dowelled connections and screwed connections proved to have high strength and stiffness. They were efficient to engage the BRBs to resist lateral loads. The BRBGF with the screwed connections had smaller initial slips compared with the BRBGF with the dowelled connections when the load was below the SLS level. However, both frames had comparable performance when the load exceeded the SLS level as the BRBs governed the system behaviour. The Eurocode 5 provided a good strength prediction for the dowelled connections but a conservative strength prediction for the screwed connections due to the friction contribution. The stiffness predictions overestimated the actual stiffness for the dowelled and screwed connections.
- The stiffness of the dowelled connections decreased after reaching their design strength. Therefore, the quality control of BRBs is essential to avoid higher overstrength than the specification. The screwed connections at the bottom had larger slips perpendicular to timber grain due to the rotation of beam-column connections and the inclined loading angle to the timber grain. To minimize the slips, 90° STS are recommended to be installed to resist the perpendicular-to-grain load.
- The connection analysis illustrated that Eurocode 5 could not provide conservative stiffness prediction on multiple fastener timber connections. The influence of connection stiffness on the system behaviour can be further studied by numerical analysis and this experimental work will provide the data for future model calibration.

Acknowledgements

The authors would like to thank the Natural Hazards Research Platform in New Zealand, QuakeCore, University of Canterbury, Shanghai Research Institute of Materials and Timber Connect Limited for partially sponsoring the project. The authors appreciate the technical support provided by Prof. Roger Nokes, technicians Russell McConchie, Alan Thirlwell, Michael Weavers and Peter Coursey from University of Canterbury.

References

[1] A. Kirstein, J. Siracusa, T. Smith, The new timber von Haast replacement building in Christchurch, 2018 NZSEE Conference (2018) 1–9.

[2] S. Hussain, P. Van Benschoten, M. Al Satari, S. Lin, Buckling Restrained Braced Frame (BRBF) Structures: Analysis, Design and Approvals Issues, in: The 75th SEAOC Annual Convention, September 13-16, 2006.

[3] C. J. Black, I. Aiken, Component Testing , Stability Analysis and Characterization of Buckling-Restrained Unbonded Braces TM University of California , Berkeley, Technical Report January 2016, Pacific Earthquake Engineering Research Center, 2002.
[4] K.-C. Tsai, J.-W. Lai, Y.-C. Hwang, S.-L. Lin, C.-H. Weng, Research and application of double-core buckling restrained braces in Taiwan, 13th World Conference on Earthquake Engineering (2004).
[5] C. Uang, M. Nakashima, K. Tsai, Research and application of buckling-restrained braced frames, International Journal of Steel Structures 4 (2004) 301–313.
[6] Q. Xie, State of the art of buckling-restrained braces in Asia, Journal of Constructional Steel Research 61 (2005) 727–748. doi:10.1016/j.jcsr.2004.11.005.
[7] G. Della Corte, M. D'Aniello, R. Landolfo, F. M. Mazzolani, Review of steel buckling-restrained braces, Steel Construction 4 (2011) 85–93. doi:10.1002/stco.201110012.
[8] C. Chou, J. Liu, D. Pham, Steel buckling-restrained braced frames with single and dual corner gusset connections: seismic tests and analyses, Earthquake engineering & structural dynamics 41 (2012) 1137–1156.
[9] K. D. Palmer, A. S. Christopulos, D. E. Lehman, C. W. Roeder, Experimental evaluation of cyclically loaded, large-scale, planar and 3-d buckling-restrained braced frames, Journal of Constructional Steel Research 101 (2014) 415–425. URL: http://dx.doi.org/10.1016/j.jcsr.2014.06.008. doi:10.1016/j.jcsr.2014.06.008.
[10] J. Wang, B. Li, C. Chou, L. Chen, Cyclic experimental and analytical studies of buckling-restrained braces with various gusset connections, Engineering Structures 163 (2018) 38–50. URL: https://doi.org/10.1016/j.engstruct.2018.02.008. doi:10.1016/j.engstruct.2018.02.008.
[11] A. Watanabe, Y. Hitomi, E. Saeki, A. Wada, M. Fujimoto, Properties of brace encased in buckling-restraining concrete and steel tube, 1988.
[12] T. Takeuchi, J. F. Hajjar, R. Matsui, K. Nishimoto, I. D. Aiken, Effect of local buckling core plate restraint in buckling restrained braces, Engineering Structures 44 (2012) 304–311. URL: http://dx.doi.org/10.1016/j.engstruct.2012.05.026. doi:10.1016/j.engstruct.2012.05.026.
[13] Y. L. Guo, J. S. Zhu, P. Zhou, B. L. Zhu, A new shuttle-shaped buckling-restrained brace. Theoretical study on buckling behavior and load resistance, Engineering Structures 147 (2017) 223–241. URL: http://dx.doi.org/10.1016/j.engstruct.2017.05.033. doi:10.1016/j.engstruct.2017.05.033.
[14] C. Avci-Karatas, O. C. Celik, C. Yalcin, Experimental Investigation of Aluminum Alloy and Steel Core Buckling Restrained Braces (BRBs), International Journal of Steel Structures 18 (2018) 650–673. URL: https://doi.org/10.1007/s13296-018-0025-y. doi:10.1007/s13296-018-0025-y.
[15] G. Q. Li, Y. Z. Sun, J. Jiang, F. F. Sun, C. Ji, Experimental study on two-level yielding buckling-restrained braces, Journal of Constructional Steel Research 159 (2019) 260–269. URL: https://doi.org/10.1016/j.jcsr.2019.04.042. doi:10.1016/j.jcsr.2019.04.042.
[16] H. Sun, M. Jia, S. Zhang, Y. Wang, Study of buckling-restrained braces with concrete infilled GFRP tubes, Thin-Walled Structures 136 (2019) 16–33. URL: https://doi.org/10.1016/j.tws.2018.10.040. doi:10.1016/j.tws.2018.10.040.
[17] W. H. Pan, J. Z. Tong, Y. L. Guo, C. M. Wang, Optimal design of steel buckling-restrained braces considering stiffness and strength requirements, Engineering Structures 211 (2020) 110437. URL: https://doi.org/10.1016/j.engstruct.2020.110437. doi:10.1016/j.engstruct.2020.110437.
[18] I. D. Aiken, S. A. Mahin, P. Uriz, Large-scale testing of buckling-restrained braced frames, in: Proceedingsof the Japan Passive Control Symposium, 2002, pp. 35–44.
[19] K. Tsai, P. Hsiao, K. Wang, Y. Weng, M. Lin, K. Lin, C. Chen, J. Lai, S. Lin, Pseudo-dynamic tests of a full-scale CFT/BRB frame—Part I: Specimen design, experiment and analysis, Earthquake Engineering & Structural Dynamics 37 (2008) 1081–1098.
[20] C. Chou, J. Liu, D. Pham, Steel buckling-restrained braced frames with single and dual corner gusset connections: seismic tests and analyses, Earthquake engineering & structural dynamics 41 (2012) 1137–1156.
[21] L. A. Fahnestock, J. M. Ricles, R. Sause, Experimental evaluation of a large-scale buckling-restrained braced frame, Journal of structural engineering 133 (2007) 1205–1214.
[22] J. W. Berman, M. Bruneau, Cyclic testing of a buckling restrained braced frame with unconstrained gusset connections, Journal of Structural Engineering 135 (2009) 1499–1510. doi:10.1061/(ASCE)ST.1943-541X.0000078.
[23] Y. J. Yu, K. C. Tsai, C. H. Li, Y. T. Weng, C. Y. Tsai, Analytical simulations for shaking table tests of a full scale buckling restrained braced frame, Procedia Engineering 14 (2011) 2941–2948. doi:10.1016/j.proeng.2011.07.370.
[24] N. NAKAMURA, T. SUZUKI, S. NAKAMURA, Three-dimensional simulation analysis of a full-scale 5-story building with steel dampers, Blucher Mech Eng Proc 1 (2012) 636–650.
[25] H. Guerrero, T. Ji, A. Teran-Gilmore, J. A. Escobar, A method for preliminary seismic design and assessment of low-rise structures protected with buckling-restrained braces, Engineering Structures 123 (2016) 141–154. URL: http://dx.doi.org/10.1016/j.engstruct.2016.05.015. doi:10.1016/j.engstruct.2016.05.015.
[26] R. Sabelli, S. Mahin, C. Chang, Seismic demands on steel braced frame buildings with buckling-restrained braces, Engineering Structures 25 (2003) 655–666. doi:10.1016/S0141-0296(02)00175-X.
[27] C. J. Black, N. Makris, I. D. Aiken, Component testing, seismic evaluation and characterization of buckling-restrained braces, Journal of Structural Engineering 130 (2004) 880–894.
[28] R. Tremblay, M. Lacerte, C. Christopoulos, Seismic response of multistory buildings with self-centering energy dissipative steel braces, Journal of structural engineering 134 (2008) 108–120.
[29] L. G. Vigh, Á. Zsarnóczay, T. Balogh, Eurocode conforming design of BRBF – Part I: Proposal for codification, Journal of Constructional Steel Research 135 (2017) 265–276. URL: http://dx.doi.org/10.1016/j.jcsr.2017.04.010. doi:10.1016/j.jcsr.2017.04.010.
[30] M. Naghavi, R. Rahnavard, R. J. Thomas, M. Malekinejad, Numerical evaluation of the hysteretic behavior of concentrically braced frames and buckling restrained brace frame systems, Journal of Building Engineering 22 (2019) 415–428. URL: https://doi.org/10.1016/j.jobe.2018.12.023. doi:10.1016/j.jobe.2018.12.023.
[31] R. Rahnavard, M. Naghavi, M. Aboudi, M. Suleiman, Investigating modeling approaches of buckling-restrained braces under cyclic loads,

Case Studies in Construction Materials 8 (2018) 476–488. URL: https://doi.org/10.1016/j.cscm.2018.04.002. doi:10.1016/j.cscm.2018.04.002.
[32] O. Atlayan, F. A. Charney, Hybrid buckling-restrained braced frames, Journal of Constructional Steel Research 96 (2014) 95–105. URL: http://dx.doi.org/10.1016/j.jcsr.2014.01.001. doi:10.1016/j.jcsr.2014.01.001.
[33] L. Di Sarno, G. Manfredi, Experimental tests on full-scale RC unretrofitted frame and retrofitted with buckling-restrained braces, Earthquake Engineering & Structural Dynamics 41 (2012) 315–333.
[34] Z. Qu, S. Kishiki, H. Sakata, A. Wada, Y. Maida, Subassemblage cyclic loading test of RC frame with buckling restrained braces in zigzag configuration, Earthquake engineering & structural dynamics 42 (2013) 1087–1102.
[35] C. Mahrenholtz, P. Lin, A. Wu, K. Tsai, S. Hwang, R. Lin, M. Y. Bhayusukma, Retrofit of reinforced concrete frames with buckling-restrained braces, Earthquake Engineering & Structural Dynamics 44 (2015) 59–78.
[36] Z. Qu, J. Xie, T. Wang, S. Kishiki, Cyclic loading test of double K-braced reinforced concrete frame subassemblies with buckling restrained braces, Engineering Structures 139 (2017) 1–14. URL: http://dx.doi.org/10.1016/j.engstruct.2017.02.040. doi:10.1016/j.engstruct.2017.02.040.
[37] A. C. Wu, K. C. Tsai, H. H. Yang, J. L. Huang, C. H. Li, K. J. Wang, H. H. Khoo, Hybrid experimental performance of a full-scale two-story buckling-restrained braced RC frame, Earthquake Engineering and Structural Dynamics 46 (2017) 1223–1244. doi:10.1002/eqe.2853.
[38] R. Ozcelik, E. F. Erdil, Pseudodynamic test of a deficient RC frame strengthened with buckling restrained braces, Earthquake Spectra 35 (2019) 1163–1187. doi:10.1193/122317EQS263M.
[39] Z. Zhang, S. N. Zhang, E. F. Deng, T. T. Zhou, Y. Yi, H. He, N. N. Li, Experimental study on seismic performance of double-level yielding buckling-restrained braced concrete frames, Archives of Civil and Mechanical Engineering 20 (2020) 1–16. doi:10.1007/s43452-020-00049-7.
[40] K.-c. Tsai, A.-c. Wu, K.-y. Pan, H.-h. Yang, Buckling Restrained Braces for Existing and New Reinforced Concrete Frames (2017).
[41] Z. Qu, S. Kishiki, Y. Maida, H. Sakata, A. Wada, Seismic responses of reinforced concrete frames with buckling restrained braces in zigzag configuration, Engineering Structures 105 (2015) 12–21. URL: http://dx.doi.org/10.1016/j.engstruct.2015.09.038. doi:10.1016/j.engstruct.2015.09.038.
[42] C. Y. Tsai, K. C. Tsai, L. W. Chen, A. C. Wu, Seismic performance analysis of BRBs and gussets in a full-scale 2-story BRB-RCF specimen, Earthquake Engineering and Structural Dynamics 47 (2018) 2366–2389. doi:10.1002/eqe.3073.
[43] Y. Khorasani, Feasibility study of hybrid wood steel structures, Ph.D. thesis, University of British Columbia, 2011.
[44] Z. Li, M. He, X. Wang, M. Li, Seismic performance assessment of steel frame infilled with prefabricated wood shear walls, Journal of Constructional Steel Research 140 (2018) 62–73. URL: https://doi.org/10.1016/j.jcsr.2017.10.012. doi:10.1016/j.jcsr.2017.10.012.
[45] M. He, Q. Luo, Z. Li, H. Dong, M. Li, Seismic performance evaluation of timber-steel hybrid structure through large-scale shaking table tests, Engineering Structures 175 (2018) 483–500. URL: https://doi.org/10.1016/j.engstruct.2018.08.029. doi:10.1016/j.engstruct.2018.08.029.
[46] H.-E. Blomgren, J.-P. Koppitz, A. D. Valdés, E. Ko, The heavy timber buckling-restrained braced frame as a solution for commercial buildings in regions of high seismicity, in: World Conference on Timber Engineering, Vienna, Austria, 2016.
[47] C. Murphy, H.-e. Blomgren, D. Rammer, Development of timber buckling- restrained braces for mass timber braced frames, International Network on Timber Engineering Research (INTER) - Meeting fifty-two, Tacoma (US) (2019) 1–14.
[48] American Institute of Steel Construction (AISC), Seismic provisions for structural steel buildings. ANSI/AISC 341-16, Chicago, IL, 2016.
[49] M. Timmers, A. Tsay Jacobs, Concrete apartment tower in Los Angeles reimagined in mass timber, Engineering Structures 167 (2018) 716–724. doi:10.1016/j.engstruct.2017.11.047.
[50] F. Zhang, X. Chen, L. Chen, Y. Leng, M. Wang, Q. Xu, Shaking table test study on a five-story post-and-beam glulam structure, in: World Conference on Timber Engineering, Seoul, Korea, 2018.
[51] C. F. Gilbert, J. Erochko, Development and testing of hybrid timber-steel braced frames, Engineering Structures 198 (2019) 109495. doi:10.1016/j.engstruct.2019.109495.
[52] M. Stepinac, V. Rajcic, R. Tomasi, F. Hunger, J.-W. G. Van de Kuilen, E. Serrano, Comparison of design rules for glued-in rods and design rule proposal for implementation in European standards, in: Proceedings of CIB-W18 meeting, Vol.46, Vancouver, Canada, 2013.
[53] H. Xiong, Y. Liu, Experimental Study of the Lateral Resistance of Bolted Glulam Timber Post and Beam Structural Systems, Journal of Structural Engineering (United States) 142 (2016) 1–11. doi:10.1061/(ASCE)ST.1943-541X.0001205.
[54] British Standard Institution (BSI), Eurocode 5: design of timber structures—Part 1-1: General—Common rules and rules for buildings, 2004.
[55] K. W. Johansen, Theory of timber connections, Int Assoc Bridge Struct Eng 9 (1949) 249–262.
[56] F. Lam, M. Schulte-Wrede, C. C. Yao, J. J. Gu, Moment resistance of bolted timber connections with perpendicular to grain reinforcements, 10th World Conference on Timber Engineering 2008 2 (2008) 978–985.
[57] K. Sawata, T. Sasaki, S. Kanetaka, Estimation of shear strength of dowel-type timber connections with multiple slotted-in steel plates by European yield theory, Journal of Wood Science 52 (2006) 496–502. doi:10.1007/s10086-006-0800-9.
[58] X. Fan, S. Zhang, W. Qu, Load-carrying behaviour of dowel-type timber connections with multiple slotted-in steel plates, Applied Mechanics and Materials 94-96 (2011) 43–47. doi:10.4028/www.scientific.net/AMM.94-96.43.
[59] J.-F. Bocquet, F. Epinal, R. Lemaître, T. K. Bader, Design recommendations and example calculations for dowel-type connections with multiple shear planes, Design of Connections in Timber Structures (2018) 241.
[60] L. M. Ottenhaus, M. Li, T. Smith, P. Quenneville, Mode Cross-Over and Ductility of Dowelled LVL and CLT Connections under Monotonic and Cyclic Loading, Journal of Structural Engineering (United States) 144 (2018) 1–10. doi:10.1061/(ASCE)ST.1943-541X.0002074.
[61] L. M. Ottenhaus, M. Li, T. Smith, P. Quenneville, Overstrength of dowelled clt connections under monotonic and cyclic loading, Bulletin of Earthquake Engineering 16 (2018) 753–773. doi:10.1007/s10518-017-0221-8.
[62] L. M. Ottenhaus, M. Li, T. Smith, Structural performance of large-scale dowelled CLT connections under monotonic and cyclic loading, Engineering Structures 176 (2018) 41–48. URL: https://doi.org/10.1016/j.engstruct.2018.09.002. doi:10.1016/j.

engstruct.2018.09.002.
[63] C. Sandhaas, J. W. G. van de Kuilen, Strength and stiffness of timber joints with very high strength steel dowels, Engineering Structures 131 (2017) 394–404. URL: http://dx.doi.org/10.1016/j.engstruct.2016.10.046. doi:10.1016/j.engstruct.2016.10.046.
[64] R. Lemaître, F. Epinal, J.-F. Bocquet, M. Schweigler, T. K. Bader, Beam-on-foundation modelling as an alternative design method for single fastener connections, Design of Connections in Timber Structures (2018) 207.
[65] R. Lemaitre, J.-F. Bocquet, M. Schweigler, T. K. Bader, Beam-on-Foundation Modelling as an Alternative Design Method for Timber Joints with Dowel-Type Fasteners–Part 2: Modelling Techniques for Multiple Fastener Connections, in: 6th INTER Proceedings, 2019: International Network on Timber Engineering Research 2019, Tacoma, USA, Karlsruher Institut für Technologie, 2019, 2019.
[66] I. Bejttka, H. Blaß, H. Blass, Joints with Inclined Screws, Proceedings of CIB-W18 Timber Structures, Meeting 35 (2002) 35–7–3.
[67] R. Tomasi, A. Crosatti, M. Piazza, Theoretical and experimental analysis of timber-to-timber joints connected with inclined screws, Construction and Building Materials 24 (2010) 1560–1571. URL: http://dx.doi.org/10.1016/j.conbuildmat.2010.03.007. doi:10.1016/j.conbuildmat.2010.03.007.
[68] M. Piazza, A. Polastri, R. Tomasi, Ductility of timber joints under static and cyclic loads, Proceedings of the Institution of Civil Engineers: Structures and Buildings 164 (2011) 79–90. doi:10.1680/stbu.10.00017.
[69] H. Krenn, G. Schickhofer, Joints with inclined Screws and Steel Plates as outer Members, in: Proceedings of the international council for research and innovation in building and construction, Working commission W18 – timber structures, Meeting 42, Duebendorf, Switzerland, 2009.
[70] M. Closen, Self-Tapping Screw Assemblies Under Monotonic Loading, Master thesis, The University of British Columbia, 2012.
[71] R. Gohlich, J. Erochko, J. E. Woods, Experimental testing and numerical modelling of a heavy timber moment-resisting frame with ductile steel links, Earthquake Engineering and Structural Dynamics 47 (2018) 1460–1477. doi:10.1002/eqe.3025.
[72] N. Vella, L. Gardner, S. Buhagiar, Experimental analysis of cold-formed steel-to-timber connections with inclined screws, Structures 24 (2020) 890–904. URL: https://doi.org/10.1016/j.istruc.2020.02.009. doi:10.1016/j.istruc.2020.02.009.
[73] M. A. H. Mirdad, Y. H. Chui, Stiffness prediction of Mass Timber Panel-Concrete (MTPC) composite connection with inclined screws and a gap, Engineering Structures 207 (2020) 110215. URL: https://doi.org/10.1016/j.engstruct.2020.110215. doi:10.1016/j.engstruct.2020.110215.
[74] U. A. Girhammar, N. Jacquier, B. Källsner, Stiffness model for inclined screws in shear-tension mode in timber-to-timber joints, Engineering Structures 136 (2017) 580–595. URL: http://dx.doi.org/10.1016/j.engstruct.2017.01.022. doi:10.1016/j.engstruct.2017.01.022.
[75] D. Moroder, Floor diaphragms in multi-storey timber buildings, Ph.D. thesis, 2016.
[76] Australia and New Zealand Standards, NZS1170.5: Structural design actions - Part 5: Earthquake actions-New Zealand, Wellington, New Zealand, 2004.
[77] D. R. Sahoo, S.-H. Chao, Performance-based plastic design method for buckling-restrained braced frames, Engineering Structures 32 (2010) 2950–2958. URL: http://dx.doi.org/10.1016/j.engstruct.2010.05.014. doi:10.1016/j.engstruct.2010.05.014.
[78] Chinese Global Standards, GB50017-2017: Code for Design of Steel Structures, China Architecture & Building Press Beijing, China, Beijing, China, 2017.
[79] New Zealand Standards, NZS3603:1993 Timber structures standard, 1993.
[80] New Zealand Standards, NZS 3404: Part 1:1997 - Steel Structure Standard, New Zealand Standards, Wellington, New Zealand, 1997.
[81] ETA(European Technical Assessment), RothoBlaas Self-tapping screws and threaded rods ETA-11 / 0030 of 2016-04-07, Technical Report 305, 2016.
[82] Rothoblaas, VGU: 45° washer for VGS - Bright zinc plated carbon steel, 2017. URL: https://www.rothoblaas.com/products/fastening.
[83] W. López, R. Sabelli, Seismic Design of Buckling-Restrained Braced Frames, Technical Report, 2004. doi:10.1139/l06-068.
[84] Chinese Global Standards, GB50010-2010: Code for design of concrete structures, China Architecture & Building Press Beijing, China, Beijing, China, 2010.
[85] American Institute of Steel Construction (AISC), ANSI / AISC 360-16, Specification for Structural Steel Buildings, 2016.
[86] K. Tsai, P. Hsiao, Pseudo-dynamic test of a full-scale CFT/BRB frame—Part II: Seismic performance of buckling-restrained braces and connections, Earthquake Engineering & Structural Dynamics 37 (2008) 1099–1115.
[87] International Organization for Standardization (ISO), Timber structures—Joints made with mechanical fasteners—Quasi-static reversed-cyclic test method, ISO16670, 2003.
[88] R. Nokes, Streams: System Theory and Design, Christchurch, New Zealand, 2017.
[89] L. M. Ottenhaus, M. Li, R. Nokes, P. Cammock, B. McInnes, Use of particle tracking velocimetry in timber material and connection testing, European Journal of Wood and Wood Products 77 (2019) 195–209. URL: http://dx.doi.org/10.1007/s00107-018-1376-y. doi:10.1007/s00107-018-1376-y.
[90] M. Dorn, Investigations on the Serviceability Limit State of Dowel-Type Timber Connections, Phd thesis, Vienna University of Technology, 2012.
[91] M. Popovski, H. G. Prion, E. Karacabeyli, Shake table tests on single-storey braced timber frames, Canadian Journal of Civil Engineering 30 (2003) 1089–1100. doi:10.1139/l03-060.
[92] T. V. Galambos, B. Ellingwood, Serviceability limit states: deflection, Journal of Structural Engineering 112 (1986) 67–84.
[93] L. G. Griffis, Serviceability limit states under wind load, Engineering Journal 30 (1993) 1–16.
[94] British Standard Institution (BSI), BS EN 12512:2001: Timber structures. Test methods. Cyclic testing of joints made with mechanical fasteners, 2002.
[95] M. Jia, D. Lu, L. Guo, L. Sun, Experimental research and cyclic behavior of buckling-restrained braced composite frame, Journal of Constructional Steel Research 95 (2014) 90–105. URL: http://dx.doi.org/10.1016/j.jcsr.2013.11.021. doi:10.1016/j.jcsr.2013.11.021.
[96] K. D. Palmer, A. S. Christopulos, D. E. Lehman, C. W. Roeder, Experimental evaluation of cyclically loaded, large-scale, planar and 3-d

buckling-restrained braced frames, Journal of Constructional Steel Research 101 (2014) 415–425. URL: http://dx.doi.org/10.1016/j.jcsr.2014.06.008. doi:10.1016/j.jcsr.2014.06.008.

[97] W. Muñoz, A. Salenikovich, M. Mohammad, P. Quenneville, Determination of yield point and ductility of timber assemblies: In search for a harmonised approach, 10th World Conference on Timber Engineering 2008 2 (2008) 1064–1071.

[98] American Society for Testing and Materials, Standard Test Methods for Cyclic (Reversed) Load Test for Shear Resistance of Vertical Elements of the Lateral Force Resisting Systems forBuildings, E2126 11 (2011) 1–15. doi:10.1520/E2126-11.2.

[99] G. A. Macrae, G. C. Clifton, Research on Seismic Performance of Steel Structures, Steel Innovations 2015 Conference (2015) 3–4.

[100] J. Ehlbeck, H. J. Larsen, Eurocode 5 - Design of timber structures: Joints, in: International Workshop on Wood Connector, Forest Products Society, 1993, pp. 9–23.

[101] R. Jockwer, A. Jorissen, Stiffness and deformation of connections with dowel-type fasteners, Design of Connections in Timber Structures (2018) 95.

[102] M. Izzi, G. Flatscher, M. Fragiacomo, G. Schickhofer, Experimental investigations and design provisions of steel-to-timber joints with annular-ringed shank nails for Cross-Laminated Timber structures, Construction and Building Materials 122 (2016) 446–457. URL: http://dx.doi.org/10.1016/j.conbuildmat.2016.06.072. doi:10.1016/j.conbuildmat.2016.06.072.

[103] C.-l. Wang, J. Lyu, J. Zhao, H. Yang, Experimental investigation of the shear characteristics of steel-to-timber composite joints with inclined self-tapping screws, Engineering Structures 215 (2020) 110683. URL: https://doi.org/10.1016/j.engstruct.2020.110683. doi:10.1016/j.engstruct.2020.110683.

[104] A. Ringhofer, Axially Loaded Self-Tapping Screws in Solid Timber and Laminated Timber Products, Verlag der Technischren Universität Graz, 2017. doi:10.3217/978-3-85125-555-3.

[105] H. J. Blaß, I. Bejtka, T. Uibel, Tragfähigkeit von Verbindungen mit selbstbohrenden Holzschrauben mit Vollgewinde, KIT Scientific Publishing, 2006.